



# Tumor-targeting nanomaterials based on metal-organic frameworks mediate tumor immunotherapy by promoting cuproptosis and pyroptosis in hepatocellular carcinoma cells

Xiaoyuan Yi<sup>a,1</sup>, Huaying Xie<sup>a,1</sup>, Kunzhao Huang<sup>a</sup>, Jianzhang Luo<sup>a</sup> , Wen Li<sup>a</sup>, Qingyu Zeng<sup>a</sup>, Feifei He<sup>a</sup>, Wuxiang Shi<sup>b</sup>, Duo Wang<sup>c,\*</sup> , Liyan Wang<sup>a,\*\*</sup> 

<sup>a</sup> Digestive Department, The Affiliated Hospital of Guilin Medical University, Lequn road No.15, Xiufeng district, Guilin, 541001, China

<sup>b</sup> Health Management Unit, Faculty of Humanities and Management, Guilin Medical University, Guilin, Guangxi, 541199, China

<sup>c</sup> Center of Interventional Radiology & Vascular Surgery, Department of Radiology, Zhongda Hospital, Medical School, Southeast University, Nanjing, 210009, China

## ARTICLE INFO

### Keywords:

Hepatocellular carcinoma  
Cuproptosis  
Pyroptosis  
Immunotherapy  
Multilayered interaction strategy

## ABSTRACT

Activating a robust immune response is an effective strategy for achieving tumor eradication. In this study, copper-based metal-organic framework nanoparticles (referred to as FA-PZ@MOF NPs), which have the ability to simultaneously induce cuproptosis and pyroptosis in tumor cells, were designed to utilize the synergistic effects of cuproptosis and pyroptosis to trigger immunogenic cell death (ICD). This can inhibit tumor growth, migration, and metastasis while enabling efficient antitumor immunotherapy. The nano inducer targets hepatocellular carcinoma tumor cells via folic acid, dissociates and releases copper ions in the tumor microenvironment (TME), which has a high glutathione concentration, leading to copper ion overload, thereby mediating cuproptosis. Additionally, the released ZnO<sub>2</sub> generates substantial amounts of H<sub>2</sub>O<sub>2</sub> and Zn<sup>2+</sup> in the acidic environment, enhancing the Cu<sup>2+</sup>-based Fenton-like reaction for chemokinetic therapy. This exacerbates the reactive oxygen species (ROS) storms and mitochondrial damage, and combined with the action of Polyphyllin VI (PPVI), induces pyroptosis and cuproptosis. This multilayered interaction strategy also triggers robust ICD while inhibiting hepatocellular carcinoma tumor metastasis and invasion.

## 1. Introduction

Copper is an essential trace metal element in human cells, with intracellular copper levels regulated by conserved homeostatic mechanisms. These mechanisms play critical roles in various biochemical processes, including antioxidant defense, mitochondrial respiration, and biosynthesis [1–3]. However, excessive accumulation of copper ions can lead to protein toxic stress [4,5], causing the aggregation of mitochondrial thioctylated proteins and destabilization of Fe-S cluster proteins, ultimately inducing cuproptosis [6,7]. As a new form of programmed cell death, cuproptosis has garnered significant attention in the treatment of cancer. Copper ions exhibit high Fenton catalytic efficiency in tumor cells [8,9], facilitating the generation of ROS that drive oxidative stress and mitochondrial dysfunction, thereby inducing ICD [10–12]. However, the ICD effect is often limited by the abundance of reducing

substances in the TME [13,14].

Pyroptosis is a distinct form of programmed cell death that functions as an inflammatory pathway by recruiting the NOD-like receptor protein 3 (NLRP3) inflammasome to activate Caspase-1, which cleaves gasdermin D (GSDMD) proteins, resulting in the rupture of the cell membrane. This leads to the release of inflammatory factors and lactate dehydrogenase [15–17]. This cascade of activation triggers a robust response, inducing the release of inflammatory cytokines from immune cells [18–20]. In turn, inflammatory factors stimulate tumor cells, initiating an immune response and triggering an antioxidant response [21,22]. Simultaneously, the immune response triggered by inflammatory factors can target tumor cells, thereby facilitating immunotherapeutic interventions against tumors [23,24]. Recent studies have shown that oxidative stress with substantial amounts of ROS can promote the activation of focal cell death and activate immune responses, thereby

\* Corresponding author.

\*\* Corresponding author.

E-mail addresses: [wangduo2022@126.com](mailto:wangduo2022@126.com) (D. Wang), [wangliyan@glmuc.edu.cn](mailto:wangliyan@glmuc.edu.cn) (L. Wang).

<sup>1</sup> These authors contributed equally to this work.

inducing ICD to promote effective immunotherapy [25–27]. In contrast, cellular juxtaposition in tumor therapy is often limited by high levels of glutathione (GSH) in the TME, which reduce the immunogenicity of induced ICD [28,29].

The core of cuproptosis relies on the excessive accumulation of copper ions in cells, leading to mitochondrial dysfunction and abnormal aggregation of key proteins, which in turn triggers cell death. Meanwhile, copper ions further exacerbate oxidative stress by promoting the generation of ROS through Fenton-like reactions, and the burst of ROS is capable of activating Caspase-1 proteins, which leads to the GSDMD cleavage and induces pyroptosis. ROS and inflammatory factors generated during pyroptosis can exacerbate the accumulation of intracellular copper ions and promote the oligomerization of copper-dependent proteins, thereby triggering cuproptosis [30,31]. In addition, pyroptosis further enhances cuproptosis-induced immune response by remodeling the TME and decreasing the activity of immunosuppressive cells (e.g., M2-type macrophages) [32]. The synergistic effect of pyroptosis and cuproptosis not only kills tumor cells directly but also inhibits tumor recurrence and metastasis by activating systemic immune responses [33]. For instance, the inflammatory signaling induced by pyroptosis in conjunction with the immunogenic effects triggered by cuproptosis markedly enhanced the infiltration and activation of effector T cells, thereby establishing sustained antitumor immunity [34]. Thus, the synergistic action of these two modes of cell death can release damage-associated molecular patterns (DAMPs) and activate ICD, thereby enhancing anti-tumor immune responses. In recent years, nanomaterials combining pyroptosis and cuproptosis for antitumor therapy have also been widely studied. The study reported that biodegradable Cu-LDH nanoparticles mediated pyroptosis and cuproptosis, while promoting cancer immunotherapy and achieving efficient tumor growth inhibition [35]. In other studies, multifunctional Cu-Pic/HA NPs were designed to activate a robust immune response for anti-tumor therapy, which effectively induced total intracellular polyamine depletion, leading to enhanced cellular pyroptosis and cuproptosis [36]. Pyroptosis and cuproptosis show a wide range of promising applications in antitumor immunotherapy, providing new strategies and perspectives for tumor therapy by inducing ICD and enhancing immune responses.

The challenges posed by cuproptosis and pyroptosis must be addressed to overcome the limitations of the TME on the ICD effect. These limitations hinder tumor immunity due to the high expression of GSH in the TME, which protects tumor cells from destruction by effectively scavenging ROS [37,38]. Another critical issue is the potential harm nanomaterials may cause to normal cells if they are not properly targeted. The active targeting of the TME by stimulus-responsive nanomaterials can specifically kill tumor cells [39,40]. Furthermore, the synergistic transformation of multiple modes of cell death can enhance antitumor therapy and amplify ICD-mediated immune responses. By inducing the release of ICD-associated antigens and DAMPs [41–43], such as calreticulin (CRT), high mobility group box 1 protein (HMGB1), and adenosine triphosphate (ATP)—the adaptive immune system can be activated, thereby converting "cold tumors" into "hot tumors". Efficient ICD is predominantly driven by necrotic tumor cells; however, therapeutic outcomes remain suboptimal due to the resistance of tumors to apoptosis and other mechanism [44–46]. In light of these challenges, there is an urgent need to develop novel drug therapies that can target tumor cells and synergistically induce multiple modes of cell death, namely cuproptosis, pyroptosis, and apoptosis, while achieving high immunogenicity.

However, the combined application of multiple modes of cell death for the treatment of tumors remains in its infancy and faces significant challenges. Therefore, we adopted an antitumor strategy based on chemodynamic therapy (CDT), which enhances the accumulation of ROS within tumor cells via the Fenton reaction mediated by metal ions. This approach depletes the highly expressed GSH in the TME and interferes with mitochondrial function, and by neutralizing tumor acidity in the TME, leads to increased infiltration of CD8<sup>+</sup> T cells to enhance

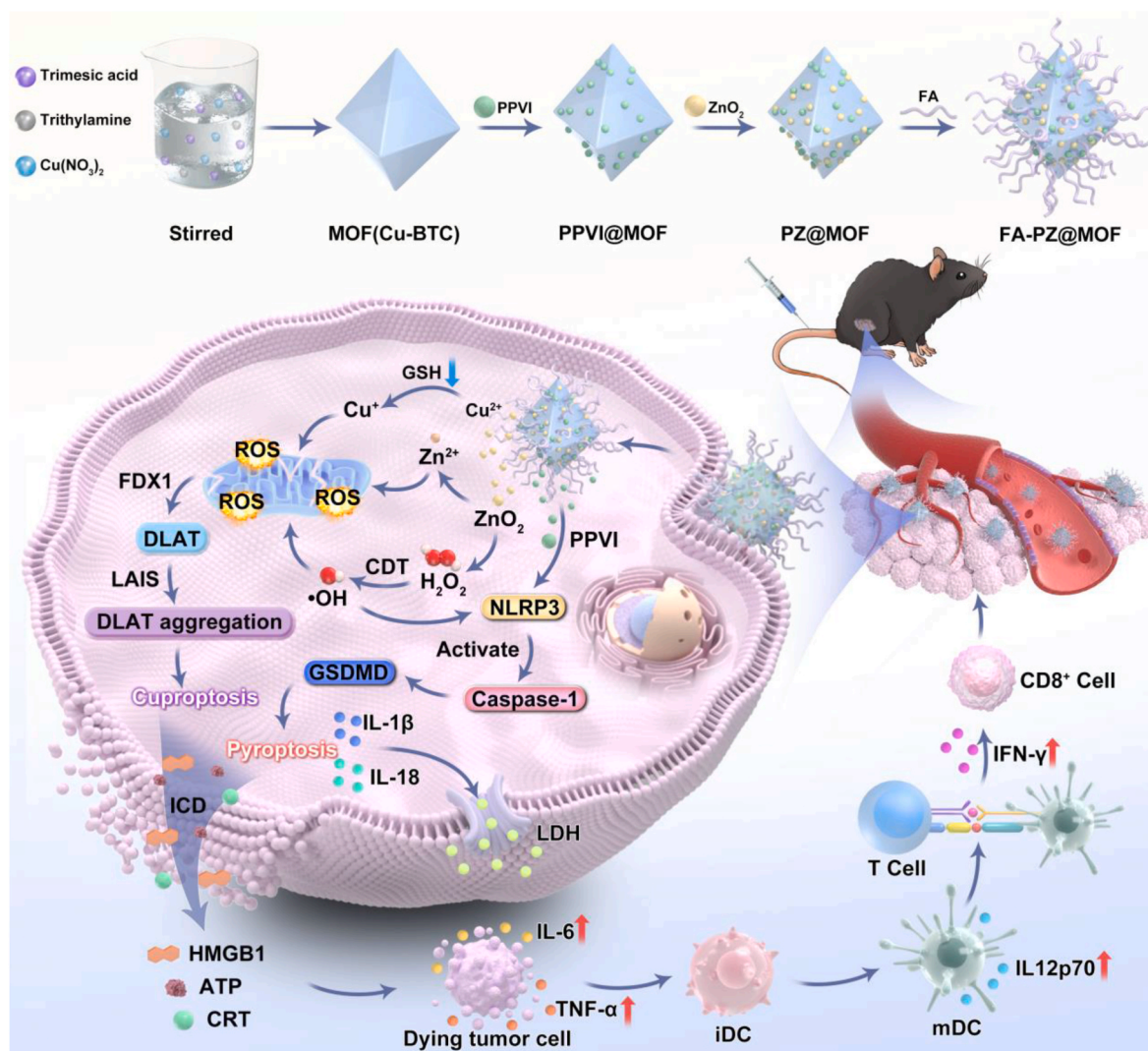
immunogenicity [47–49]. The introduction of exogenous copper further disrupts the tricarboxylic acid (TCA) cycle while eliciting a CDT response. Additionally, it enhances intracellular ROS oxidative stress through the catabolism of H<sub>2</sub>O<sub>2</sub> [2,50,51]. The accumulated ROS activates pyroptosis, upregulating the expression of the GSDMD family of proteins, inducing cell membrane rupture, and causing cellular swelling and the formation of large vesicles. Concurrently, oxidative stress driven by ROS and the accumulation of copper ions trigger cuproptosis, leading to apoptosis through multiple cellular pathways, thereby maximizing efficacy [32,52,53].

PPVI is an active saponin, which is mainly isolated from the traditional medicinal plant *Paris polyphylla*. PPVI has effective anti-cancer effects by inducing pyroptosis, apoptosis and autophagy. However, PPVI has poor bioavailability in vivo, fast metabolism, and causes reactions such as hepatotoxicity, so its drug application is limited to some extent [54,55]. Herein, we have designed a multifunctional copper-based metal-organic framework nanoparticle (FA-PZ@MOF NPs), as illustrated in Scheme 1, which integrates heavy-building PPVI, ZnO<sub>2</sub>, and folic acid (FA). This design aims to enhance drug availability while improving the biological safety through targeted tumor pathway delivery. FA ensures effective tumor targeting and cycling ability of FA-PZ@MOF NPs in vivo, leading to the intracellular release of Cu<sup>2+</sup>, ZnO<sub>2</sub>, and PPVI. ZnO<sub>2</sub> and PPVI are then exposed to a weakly acidic environment, and further generate H<sub>2</sub>O<sub>2</sub> and Zn<sup>2+</sup> in the weakly acidic environment, which enhances the Fenton-like oxygen reaction of Cu<sup>2+</sup> in the GSH-enriched tumor environment. Simultaneously, the accumulation of Zn<sup>2+</sup> and Cu<sup>+</sup> exacerbates the ROS storm and mitochondrial damage, leading to the aggregation of thioctanoylated proteins, destabilization of Fe-S clustered proteins, and induction of copper-induced cell death. Furthermore, inflammasomes are recruited as a result of the substantial generation of ROS and the synergistic effect of PPVI. Moreover, under the influence of high levels of ROS and PPVI, NLRP3 is recruited and activates Caspase-1, which further cleaves the GSDMD protein, leading to cell membrane rupture and the activation of the pyroptosis pathway. Then, the enhancement of cuproptosis, pyroptosis, and tumor apoptosis subsequently leads to the release of DAMPs from tumor cells, thereby activating the tumor immune response in vivo. Furthermore, the recruitment of immune cells exerts additional inhibitory effects on tumor metastasis and proliferation, showcasing promising antitumor therapeutic efficacy. This study unveils a novel pathway for the exploration of immunotherapy strategies in hepatocellular carcinoma.

## 2. Materials and methods

### 2.1. Materials

1,3,5-triethylamine acid (98 %), copper nitrate trihydrate (99.9 %), PolyphyllinVI were purchased from Shanghai Macklin. Zinc acetate, triethylamine, Polyvinylpyrrolidone (PVP) were obtained from Aladdin Reagent (Shanghai) Co, Ltd. DSPE-PEG-FA(MW 2000) was procured from Chongqing Yusi Pharmaceutical Technology Co., Ltd. 3,3',5,5'-Tetramethylbenzidine (TMB) and 5,5'-dithiobis (2-nitrobenzoic acid) (DTNB) were purchased from Macklin (Shanghai, China). Cell counting kit-8 (CCK-8) was provided by Zoman Biotechnology (Beijing, China). Enhanced mitochondrial membrane potential assay kit with JC-1, Calcein-AM/PI Cell Viability/Cytotoxicity Assay Kit, GSH/GSSG assay kit, ATP Assay Kit, 2,7-dichlorodihydrofluorescein (DCFH-DA) probes, Hydrogen Peroxide Assay Kit, Alexa Fluor 488-labeled, Cy3-labeled secondary antibodies, One Step TUNEL Apoptosis Assay Kit, Western Blot transfer buffer, and QuickBlock™ blocking buffer for Western blot were purchased from Beyotime Biotechnology (Shanghai, China). Hoechst 33342 and Cell Copper Content Assay Kit were obtained via Solarbio Science & Technology Co., Ltd (Beijing, China). Annexin V-FITC/PI kit was purchased from Bestbio (Shanghai, China) Transwell® with 8.0 μm Pore Polycarbonate Membrane Insert and Corning®



**Scheme 1.** Schematic representation of the molecular mechanisms by which FA-PZ@MOF NPs to activate anti tumor immunotherapy by inducing enhanced cuproptosis and pyroptosis.

Matrigel® Basement Membrane Matrix were provided by Corning Incorporated Company provided. Fluorescent secondary antibody conjugated with DyLight™ 680 was procured from Cell Signaling Technology. Cell-Light EdU Apollo567 In Vitro Kit was gotten from Guangzhou RiboBio Co., Ltd. ThiolTracker™ Violet was obtained via ThermoFisher, cat. Zinquin was provided by Shanghai Maokang Biotechnology Co., LTD (Shanghai, China). IL-6 ELISA Kit, TNF- $\alpha$  ELISA Kit, IL-1 $\beta$  ELISA kit, IL-18 ELISA kit, IL-12p70 ELISA kit and IFN- $\gamma$  ELISA kit were purchased from NeoBioscience Biotechnology Co., LTD. PerCP/Cya-nine5.5 anti-mouse CD3, APC anti-mouse CD8, FITC anti-mouse CD86, PE anti-mouse CD80 and APC anti-mouse CD11c were purchased from BioLegend.

## 2.2. Synthesis of FA-PZ@MOF NPs

First step, MOF (Cu-BTC) was synthesized according to the method in Ref. [56], then the product was washed three times with ethanol to remove the unreacted reagent and finally dried for powder storage MOF (Cu-BTC). At the same time, a PVP-modified ZnO<sub>2</sub> NPs was synthesized by dissolving 0.1 g of Zinc acetate and 0.1 g of PVP in 5.0 mL of water. Then, 0.5 mL H<sub>2</sub>O<sub>2</sub> (30 % wt in H<sub>2</sub>O) was quickly added and stirred vigorously. After 24 h of the reaction, the resulting pvp-modified ZnO<sub>2</sub> NPs was washed several times, dried and stored in a powder. Next, MOF

(2 mg) and PPVI (1 mg) were added into 2 mL of anhydrous ethanol. After stirring the mixture for 12 h, ZnO<sub>2</sub> (2 mg) was added to the above solution and kept stirring for overnight. Last, DSPE-PEG-FA (1 mg) was added and stirred for 12 h. All these procedures were carried out at room temperature. After centrifugation with anhydrous ethanol and deionized water, the final product (FA-PZ@MOF NPs) was collected and stored at -20 °C.

## 2.3. Characterizations

The morphologies of the samples were investigated by field emission scanning electron microscopy (SEM) and transmission electron microscopy (TEM) with an energy dispersive spectrum (EDS) detector. The particle size and zeta potential of FA-PZ@MOF NPs were measured by dynamic light scattering (Malvern Zetasizer). X-ray photoelectron spectroscopy (XPS) was utilized to analyze the valence state of Cu and Zn. The quantified measurement of  $\bullet$ OH was conducted by an ESR spectrometer (JEOL FA-200). The absolute contents of Cu and Zn in FA-PZ@MOF NPs were measured with an inductively coupled plasma-atomic emission spectrometry (ICP-MS, ThermoFisher, USA). The presence of PPVI in the NPs was determined by high-performance liquid chromatography (HPLC) spectroscopy (Agilent, 1290II, USA). The POD-like and GSHOx-like activity test of MOF, PPVI@MOF, PZ@MOF and

FA-PZ@MOF NPs were detected using ultraviolet–visible spectrometers (Metash, UV-5500PC). Microplate reader (Tecan, Switzerland) at a wavelength of 560 nm was used to detect the Capacity to Produce H<sub>2</sub>O<sub>2</sub>.

#### 2.4. Release behaviors of FA-PZ@MOF NPs

To investigate the release behaviors of Zn, Cu, PPVI in FA-PZ@MOF NPs, the HEPES (pH 7.4), HEPES (pH 5.4) was used to simulate tumor environments in vivo. 1 mL FA-PZ@MOF NPs was added into a dialysis bag (Mw: 3500 Da), which was then placed in 10 mL of the release medium. The bag was dialyzed at 37 °C with shaking at 100 rpm. At predetermined time, 10 mL of the released medium was removed and replaced with 10 mL of fresh medium. The cumulative release of Zn and Cu were monitored using ICP-MS (ThermoFisher, USA), and the cumulative release of PPVI was detected by HPLC spectroscopy (Agilent, 1290II, USA).

#### 2.5. Cell lines and animals

Hepa1-6 and Hepa1-6-Luc1 liver cancer cell lines were obtained from Zhejiang Meisen Technology Co.Ltd. The THLE-2 cell line was obtained from the American Type Culture Collection. Hepa1-6-Luc1 and Hepa1-6 cells were cultured in Dulbecco's modified Eagle's medium (DMEM) supplemented with 10 % fetal bovine serum (FBS) and 1 % penicillin/streptomycin. The cells were maintained in a humidified atmosphere at 37 °C with 5 % CO<sub>2</sub>.

C57BL/6 mice (4-week-old) were sourced from the Experimental Animal Center of Guilin Medical University. The animal experiments were maintained and approved by Guilin Medical University's Ethical Committee.

#### 2.6. Cellular uptake assessment

To investigate the endocytosis of FA-PZ@MOF NPs, FA-PZ@MOF NPs was modified with fluorescent molecular RhodamineB. Hepa1-6 cells on coverslips of in 24-well plate  $3 \times 10^4$  cells per well) were cultured at 37 °C for 24 h, The uptake behavior of FA-PZ@MOF NPs by Hepa1-6 cells was evaluated using flow cytometry (FCM) and inverted fluorescence microscopy (Axiovert.A1, GER). Briefly, Hepa1-6 cells were incubated with RhB labeled FA-PZ@MOF NPs for various durations (0, 1, 2, 4, and 8 h) to investigate time-dependent uptake. After staining with Hoechst 33342 (10 µg/mL) for 10 min and Cytoskeletal staining reagents for 1 h, all the treated cells were examined by Confocal Laser Scanning Microscopy (CLSM).

#### 2.7. Cytotoxicity assay

Hepa1-6 and THLE-2 cells were seeded in a 96-well plate ( $5 \times 10^3$  cells per well) and incubated overnight at 37 °C. Then, the cells were treated with the indicated MOF, PPVI@MOF, PZ@MOF and FA-PZ@MOF NPs at varying concentrations ranging from 0 to 200 µg/mL at 37 °C for 24h. Afterwards, 10 µL Cell CCK-8 solution were added into each well and co-incubation for another 2h, the relative cell viability was analyzed using a microplate reader (Tecan, Switzerland) at a wavelength of 450 nm.

#### 2.8. Intracellular ROS detection

Hepa1-6 cells were seeded in a 24-well plates ( $4 \times 10^4$  cells per well) and allowed to grow for 24 h. Subsequently, these cells were exposed to corresponding medicine for 8h. Then, these treated cells were stained by DCFH-DA (10 µM) probe for 20 min. Fluorescence intensity was measured using FCM. For fluorescence microscopy, cell samples were stained with Hoechst 33342 for 10 min, then washed twice with PBS. The stained samples were visualized under a fluorescence microscope to evaluate intracellular ROS level.

#### 2.9. Detection of mitochondrial membrane potential changes

For mitochondrial integrity assay, Hepa1-6 cells were initially seeded in 24-well plates ( $4 \times 10^4$  cells per well) and incubated overnight. Subsequently, the cells were subjected to different treatments as follows: G1:PBS, G2:MOF, G3:PPVI, G4:PPVI@MOF, G5:PZ@MOF, G6: FA-PZ@MOF NPs. After removing the original medium, JC-1 staining solution was introduced and incubated for 30 min at 37 °C. Then the cells were washed twice with JC-1 staining buffer to eliminate any unbound dye. The changes in mitochondria were subsequently observed using inverted fluorescence microscopy and photographed by fluorescence microscopy in the green channel for J-monomer and red channel for J-aggregates separately.

#### 2.10. EdU cell proliferation experiment

Hepa1-6 cells with a density of  $2 \times 10^4$  cells per well were cultured in a 48-well plate for 24h to allow the attachment of cells. The cells were subjected to various treatments and incubated for 24 h. Cell proliferation was then assessed using an EdU kit according to the manufacturer's instructions. The cells were fixed with 4 % paraformaldehyde, and EdU reagent was used to label proliferating cells, while Hoechst 33342 (10 µg/mL) was used to stain the nuclei. Stained cells were imaged using an inverted fluorescence microscope. The number of EdU-positive cells was quantified using ImageJ software to evaluate cell proliferation under different treatment conditions.

#### 2.11. Live/dead cell staining experiments

Hepa1-6 cells with a density of  $1 \times 10^5$  cells per well were cultured in a 6-well plate for 24 h to allow the attachment of cells. Afterwards, the cells were treated with the following groups: PBS, MOF, PPVI, PPVI@MOF, PZ@MOF, FA-PZ@MOF. Then, cells were incubated at 37 °C under 5 % CO<sub>2</sub> for 24 h. After treatment, the culture medium was removed, and the cells were washed with PBS. The cells were stained with Calcein AM and PI for 20 min, and finally observed by fluorescence microscope.

#### 2.12. Immunofluorescence staining

Hepa1-6 cells were cultured in confocal specific dishes for about 24 h, Following this incubation period, the cells were subjected to the specified treatments. After treatment, the cells were washed three times with PBS, fixed with 4 % paraformaldehyde for 30 min, washed with PBS three times, and incubated in the blocking solution for 30 min to block the non-specific antibody binding. The cells were then incubated overnight at 4 °C with primary antibodies. Subsequently, incubation with secondary antibody labeled by alexa flour 488 or Cy3-conjugated for 1 h was carried on, and then Hoechst 33342 was used to stain the nuclei. CLSM was used to capture fluorescence images and relative fluorescence intensity was semi-quantified using ImageJ software.

#### 2.13. Western blot assay

Hepa1-6 cells were seeded in 6-well plates ( $2 \times 10^5$  cells per well) for 24 h to allow the attachment of cells. Six groups (Control, MOF, PPVI, PPVI@MOF, PZ@MOF, FA-PZ@MOF) were set and incubated for 8 h with drugs. The original medium was discarded, the cells were washed by PBS. RIPA lysate were added to extract the protein, which was then quantified using a microvolume ultraviolet–visible spectrophotometer (Thermo Science™NanoDrop™One, USA). Equal amounts of protein (25–50 µg) from each sample were resolved on a PAGE gel, subjected to electrophoresis at 200 V for 30 min, and transferred to a PVDF membrane at 400 mA for 15–70 min. The membrane was blocked with QuickBlock™ blocking buffer for 30 min and then incubated overnight at 4 °C with primary antibodies. Following primary antibody

incubation, the membrane was washed and incubated with fluorescent secondary antibodies conjugated with DyLight™ 680.  $\beta$ -actin was used as a loading control. Protein expression was visualized using an Odyssey DLx near-infrared dual-color laser imaging system (Gene Company Limited, China).

#### 2.14. Cell pyroptosis observation by bio-SEM

Hepa1-6 cells were seeded in 24-well plates containing cell slides at the bottom of each well, and then they were treated with PBS, FA-PZ@MOF for 12 h. Afterwards, the media were discarded and treated cells were washed three times with PBS, and then 2.5 % special pentane was injected. Furthermore, the cells-carrying slides were fixed with dialdehyde fixative at 4 °C for 12h, and the slides were rinsed 3 times with phosphoric acid rinsing solution, and fixed with 1 % osmium acid for 2 h at 4 °C. Subsequently, they were rinsed 3 times with double distilled water, and experienced ethanol gradient dehydration, isoamyl acetate replacement and critical point drying in turns. After drying, they were coated with the ion sputtering instrument and then were placed on the scanning electron microscope platform. Ultimately, the slides were transferred into the sample chamber scanning electron microscope (HITACHI Regulus 8100) for observation.

#### 2.15. TUNEL staining analysis

Hepa1-6 cells with a density of  $2 \times 10^4$  cells per well were cultured in a 48-well plate for 24h to allow the attachment of cells. After treatment, the cells were washed with PBS, fixed with 4 % paraformaldehyde for 30 min, and 0.3 % TritonX-100 PBS solution was used for permeabilization. Subsequently, 100  $\mu$ L of TUNEL assay solution was added to each well. The cells were then incubated at 37 °C in the dark for 1 h, followed by three washes with PBS to remove any unbound reagents. The apoptotic cells identified by DNA fragments were observed using inverted fluorescence microscopy.

#### 2.16. Detection of cell apoptosis

Hepa1-6 cells were cultured in 6-well plates at a density of  $1 \times 10^5$  cells per well and incubated for 24 h. Following this incubation, the cells were subjected to various treatments. After treatment for 24 h, and then harvested with trypsin (EDTA absent) with PBS washing, centrifuged, and resuspended to obtain a single-cell suspension. For apoptosis analysis, cells were stained with 5  $\mu$ L of Annexin V-FITC solution for 10 min at 4 °C in the dark, followed by 10  $\mu$ L of PI solution for 5 min at 4 °C, Apoptotic cells were quantified using a flow cytometer.

#### 2.17. GSH assay/GSH and GSSG content

To detect the GSH content in Hepa1-6 cells, the cells were seeded in 24-well plates and incubated for 24 h. And then, following this, cells were subjected to various treatments. After that, the cells were stained with ThiolTracker™ Violet dye (20  $\mu$ M) for 30 min in the dark, and they were washed with PBS once. At last, intracellular fluorescence was examined by fluorescence microscope.

Hepa1-6 cells were seeded in 6-well plates at a density of  $2 \times 10^5$  cells per well incubated overnight at 37 °C. Then, the cells were treated with various treatments as per the experimental design and the intracellular GSH content was measured by GSH and GSSG detection kits.

#### 2.18. Migration assay

Migration assays were performed in transwell chambers with 8  $\mu$ m polycarbonate membranes. Hepa1-6 cells in serum-free medium were seeded into the upper chambers at a density of  $2 \times 10^4$  cells per chamber and 10 % FBS was added to the lower chambers as a chemo-attractant. After incubating for 24 h, cells that migrated through the

membrane were fixed with 4 % paraformaldehyde, stained with 0.5 % crystal violet, photographed using an inverted microscope, and quantified using ImageJ software.

#### 2.19. Colony formation assay

For the colony formation assay, Hepa1-6 cells were cultured in 6-well plates at a density of 500 cells per well and cultured in complete growth medium with corresponding treatment at 37 °C for 14 days, fixed with 4 % paraformaldehyde, stained with 0.5 % crystal violet, and counted using ImageJ software.

#### 2.20. Wound-healing assays

For wound healing evaluation, Hepa1-6 cells were seeded in 6-well plates and cultured until reaching 85 % confluence. A standardized wound was created in the cell monolayer by scraping with a 10  $\mu$ L pipette tip. Following the wound creation, cells were washed twice with PBS and cultured in serum-free medium with corresponding treatment. Wound closure was monitored under an inverted microscope at 0, 24, and 48 h. The gap area filled by cells was analyzed and measured using ImageJ software.

#### 2.21. Detection of ATP

Hepa1-6 cells were seeded in 6-well plates and subjected to different treatments. After 24 h, the supernatant and cells were collected separately, centrifuged, and extracellular ATP levels were measured using an ATP assay kit according to the manufacturer's instructions.

#### 2.22. Lactic dehydrogenase (LDH) assays

Hepa1-6 cells were seeded in a 96-well plate ( $5 \times 10^3$  cells per well) and incubated overnight at 37 °C. Then, the cells were treated with various treatments and set up a positive control (no drug and only media) for 23h, then used LDH Cytotoxicity assay kit according to the anufacturer's instruction and convert LDH into colored substance formazan which measured at a wavelength of 490 nm, and the absorbance was associated linearly with the content of LDH.

#### 2.23. In vivo fluorescence imaging of tumors

After the subcutaneous tumor model was successfully established, the tumor-bearing C57BL/6 mice were injected via the tail vein with PZ@MOF/Cy5.5 and FA-PZ@MOF/Cy5.5 (1mg/mL, 100  $\mu$ L), and fluorescence imaging of mice was conducted at different time points (0, 1, 2, 4, 8, 12, 24 h) with using the infrared imaging system. At 24 h, the mice were sacrificed, and tumors and primary organs including the heart, liver, spleen, lung, and kidney were collected for ex vivo fluorescence imaging.

#### 2.24. Bioluminescence imaging

Bioluminescence imaging (PerkinElmer, USA) was used to detect the size of tumor volume in mice. A volume of 20  $\mu$ L Luc1 Substrate (DTZ Solution) was injected intraperitoneally into tumor-bearing C57BL/6 mice. After 5 min, the mice were anesthetized with Tribromoethanol (EasyCheck, Nanjing AIBI Bio-Technology Co., Ltd). Finally, the mice were photographed in the loading room, and the images were saved.

#### 2.25. In vivo treatment Experiment

Hepa1-6(Lucl) cells concentration was adjusted to  $1 \times 10^7$  cells/100  $\mu$ L and implanted subcutaneously in mice. After that, the treatment was initiated when the tumor reached 8 mm in length. Mice were randomly divided into six groups (n = 5): G1: PBS, G2: MOF, G3: PPVI, G4:

PPVI@MOF, G5:PZ@MOF, G6: FA-PZ@MOF. The mice were injected with different formulations via the tail vein on days 0, 3, 6, 9, 12. Tumor size and weight were monitored throughout the treatment period. The tumor volume formula was given as follows: tumor volume =  $L \times W^2 \times 0.5$ , where L is the longest diameter and W is the perpendicular dimension. Changes in tumor volume were also assessed using bioluminescence imaging (PerkinElmer, USA). All mice were sacrificed on the 16th day, tumors and main organs were collected, weighed and photographed. Subsequently, the tissue sections were fixed with formaldehyde and embedded in paraffin for histological analysis. These sections were subjected to immunohistochemical or immunofluorescence staining with hematoxylin-eosin (H&E), TUNEL, Ki67, CRT and NLRP3, Caspase-1, GSDMD, DLAT, CD8, respectively, and then were observed under an optical or fluorescent inverted microscope. As well, another 60 mice were divided into the same groups (n = 10) as mentioned above and received the corresponding treatments for survival analysis and observed for 48 days. When the tumor volume reached up to 2000 mm<sup>3</sup> or premature death of mice occurred, this time was designed as the end point.

### 2.26. Biological safety evaluation

To confirm the biosafety evaluation of FA-PZ@MOF was performed on 4-week health C57BL/6 mice (n = 3) in vivo. Mice were injected intravenously with FA-PZ@MOF at a dose of 5 mg/kg (three times in total). After a 2-week period, the mice were euthanized, and blood samples were collected for routine hematological and biochemical analysis. This included tests for liver and kidney function (ALT, AST, UREA, LDH1, CREA, total bilirubin), as well as white blood cell count, red blood cell count, platelet count, and other relevant parameters. As well, major organs were fixed in 4 % formalin solution and embedded in paraffin for histological analysis. After that, these sections were stained with H&E and observed under an optical inverted microscope.

### 2.27. Hemolytic test

Blood cells were obtained from the mice and incubated with different concentrations (0, 25, 50, 75, 100, 150 and 200 µg/mL) of FA-PZ@MOF, where the PBS and pure water were separately used as negative and positive controls. Then, the supernatant was centrifugally collected (3500 rpm, 10 min) and the absorbance at 540 nm was measured through Microplate reader. The hemolysis rate can be calculated according to formula: Hemolysis rate (%) =  $(A - A_0)/(A_{\infty} - A_0) \times 100 \%$ . Where A, A<sub>0</sub> and A<sub>∞</sub> are the absorbance of the groups of experimental medicine, PBS and DI water, respectively.

### 2.28. Cytokine detection

Venous blood was obtained from the orbit of mice after different treatments, and clotted for 30 min, then centrifuged for 10 min at 3000 rpm. Finally, the serum samples were isolated and used for analysis. The serum levels of IL-18, IL-12p70, IL-1β, TNF-α, IFN-γ and IL-6 were measured with ELISA kits according to the manufacturer's instructions.

### 2.29. Flow cytometric analysis

After the treatment, the mice were euthanized, inguinal lymph nodes from tumor-bearing mice were excised and placed in 1 mL RPMI-1640 medium. The lymph nodes were homogenized using the plunger of a 1 mL syringe until the suspension became turbid. The resulting cell suspension was filtered through a 40 µm cell sieve to remove tissue debris and then centrifuged at 800 g for 5 min. The cells were resuspended in 5 % BSA solution and incubated for 15 min to block non-specific binding. Subsequently, the cells were stained with CD11c, CD80, and CD86 antibodies for 30 min in the dark. Flow cytometric analysis was performed to evaluate the activation of dendritic cells

(DCs) in the lymph nodes.

For the analysis of immune cells infiltration in tumor tissues, tumors were excised and minced in 2 mL PBS. The tissues were further digested with type IV collagenase (1 mg/mL), hyaluronidase (0.2 mg/mL), and DNase I (0.2 mg/mL) for 1 h at 37 °C in a water bath. After digestion, the suspension was filtered through a 40 µm cell sieve and centrifuged at 800 g for 5 min. The cell pellet was then mixed with Percoll at a 2:1 ratio, layered onto a Percoll gradient, and centrifuged at 20 °C for 20 min. The interface containing the viable cells was collected, washed with PBS, and blocked with 5 % BSA for 15 min. The single-cell suspension was then stained with anti-CD3 and anti-CD8 antibodies for 30 min. FCM was employed to assess immune cells infiltration within the tumor.

### 2.30. Statistical analysis

All values are expressed as mean ± standard deviation (SD), statistical analyses were conducted using GraphPad Prism software (version 9). One-way or two-way analysis of variance (ANOVA) or t-tests were used for inter-group comparisons. Data were presented as mean ± standard deviation (SD). Difference was considered to be significant if P < 0.05 (\*p < 0.05, \*\*p < 0.01, \*\*\*p < 0.001, \*\*\*\*p < 0.0001, ns indicates no significant).

## 3. Results and discussion

### 3.1. Synthesis and characterization of FA-PZ@MOF NPs

PZ@MOF NPs were prepared using a one-pot method [56], and then modified with FA to obtain FA-PZ@MOF NPs. Transmission electron microscopy (TEM) images showed that the MOF (Cu-BTC) presented a prismatic octahedral shape (Fig. 1A) and the ZnO<sub>2</sub> presented the small monodisperse and spherical granulate (Fig. S1, Supporting Information). The successfully loaded FA-PZ@MOF NPs retained the regular morphology of the MOFs (Fig. 1B; Fig. S2, Supporting Information), with fine granular materials loaded onto the MOFs' surface. High-angle annular dark-field scanning transmission electron microscopy (HAADF-STEM) images further confirmed the uniform distribution of Cu, Zn, C, O, and N elements in the FA-PZ@MOF NPs (Fig. 1C). Dynamic light scattering analysis showed that the average particle size of the FA-PZ@MOF NPs was 199.05 ± 1.405 nm (Fig. 1D). In addition, the negligible size variation of FA-PZ@MOF in both water and 10 % FBS + DMEM solution at various time points indicate that indicating the good stability of FA-PZ@MOF NPs (Fig. S3, Supporting Information). While zeta potential measurements indicated that the surface charge of the NPs varied with the successful loading of PPVI, ZnO<sub>2</sub>, and FA (Fig. S4, Supporting Information). X-ray photoelectron spectroscopy (XPS) analyses confirmed the presence of the Cu, Zn, C, O, and N elements in FA-PZ@MOF NPs (Fig. 1E). The presence of Cu<sup>2+</sup> was confirmed through high-resolution spectral fitting of the Cu2p peaks in Fig. 1F and G. Additionally, the typical diffraction peaks of ZnO<sub>2</sub> in Fig. 1H indicated that ZnO<sub>2</sub> was successfully encapsulated in the FA-PZ@MOF NPs. Finally, the FA-PZ@MOF NPs were analyzed using HPLC and ICP-MS. The loadings of PPVI, ZnO<sub>2</sub> and copper in FA-PZ@MOF nanoparticles were approximately 16.94 %, 49.6 % and 28.9 %, respectively. In conclusion, the results demonstrate the effective loading of PPVI and ZnO<sub>2</sub> as well as the successful modification of FA. These results not only prove the successful assembly of FA-PZ@MOF NPs but also lay the foundation for their potential applications in subsequent TME responses.

Subsequently, we simulated the weakly acidic environment of the TME in vitro to investigate the tumor-specific release profiles of drugs and metals from the nanomaterials. The cumulative release rates of PPVI, Zn<sup>2+</sup>, and Cu<sup>2+</sup> in phosphate buffer solution (PBS) at pH 5.4 over 24h were 72.48 %, 85.86 %, and 15.03 %, respectively (Fig. 1I–K). These rates were significantly higher than those observed in PBS at pH 7.4, confirming the targeted release in the tumor microenvironment and demonstrating their stability in the blood. The loaded ZnO<sub>2</sub> exhibited a

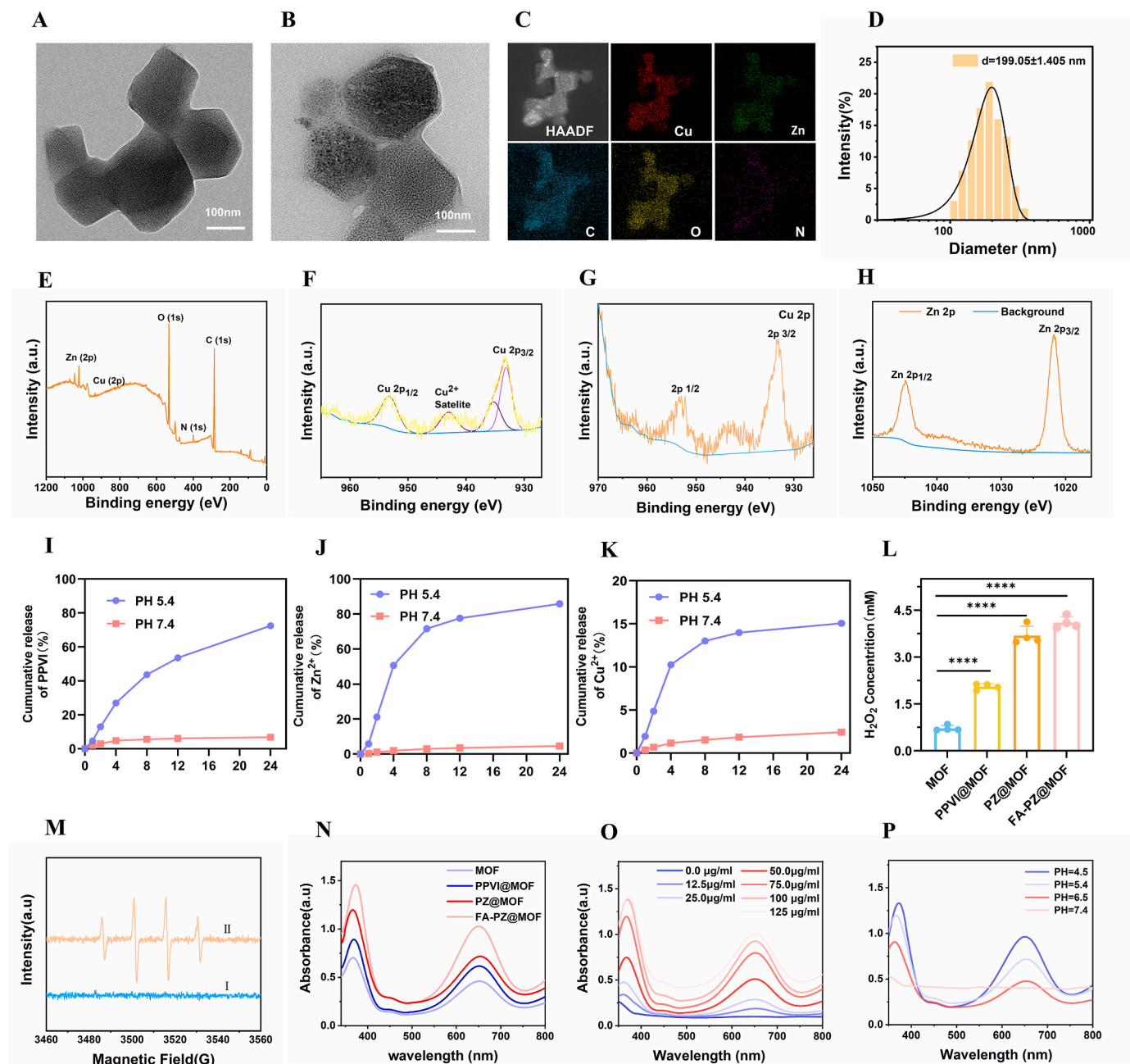


**Fig. 1.** Synthesis and characterizations of FA-PZ@MOF NPs. TEM images of MOF(A) and FA-PZ@MOF NPs (B)(scale bars: 100 nm); (C) High-angle annular dark field-scanning transmission electron microscopy (HAADF-STEM) image and elemental mapping of FA-PZ@MOF NPs (scale bars: 250 nm). (D) Particle size distribution of FA-PZ@MOF NPs. (E) XPS spectra of FA-PZ@MOF NPs. (F–G) Cu 2p XPS spectra and (H) Zn 2p XPS spectrum of FA-PZ@MOF NPs. (I) PPVI release and (J)  $Zn^{2+}$  release and (K)  $Cu^{2+}$  from FA-PZ@MOF NPs under different conditions. (L)  $H_2O_2$ -generating ability under various treatments. (M) Electron spin resonance spectra illustrating  $\cdot OH$  generation of FA-PZ@MOF NPs (I, pH 7.4; II, pH 4.5); (N) UV–vis spectra of TMB in the presence of  $H_2O_2$  and MOF, PPVI@MOF, PZ@MOF, FA-PZ@MOF NPs; (O) UV–vis spectra of TMB in the presence of  $H_2O_2$  and FA-PZ@MOF NPs under different concentrations and (P) Different pH values.

remarkably strong  $H_2O_2$ -donating capacity, which effectively improved the  $H_2O_2$ -limited Fenton reaction in tumor cells. By examining the  $H_2O_2$  production of different materials under acidic conditions, we confirmed that the modification of  $ZnO_2$  significantly increased  $H_2O_2$  production (Fig. 1L), thereby promoting the  $Cu^{2+}$ -based Fenton-like reaction. Owing to the substantial production of  $H_2O_2$  in FA-PZ@MOF NPs, we systematically evaluated the generation of  $\cdot OH$  radicals using electron spin resonance (ESR) spectroscopy. In this study, 5,5-dimethyl-1-pyrroline N-oxide (DMPO) was employed as a spin-trapping agent for  $\cdot OH$  radicals. As depicted in Fig. 1M, no significant  $\cdot OH$  signal was detected for FA-PZ@MOF NPs in PBS at pH 7.4. Conversely, a distinct and

characteristic ESR signal was observed under acidic conditions at pH 4.5. Next, the enhanced peroxidase-like (POD-like) activity of FA-PZ@MOF NPs was confirmed using TMB colorimetric assays (Fig. 1N). Upon mixing various concentrations of FA-PZ@MOF NPs with  $H_2O_2$  and TMB, the absorbance of the solution exhibited a significant concentration-dependent increase (Fig. 1O). We confirmed that under low pH, a higher TMB concentration, a higher  $H_2O_2$  concentration, strong POD-like activity was observed (Fig. 1P; Fig. S5, Supporting Information). Since the overexpression of GSH in the TME affects the therapeutic efficacy of tumors, the glutathione depleting capacity was further evaluated to verify the glutathione-like (GSH-like) activity using

the GSH detection reagent DTNB. A significant reduction in the characteristic peak at 415 nm was observed following treatment, demonstrating a distinct acidic-induced and concentration-dependent decreasing trend (Fig. S6, Supporting Information).

### 3.2. Cellular uptake and depletion mechanisms

The aforementioned experiments highlighted the diverse and specific enzymatic activities of FA-PZ@MOF NPs, thereby providing a strong impetus for further investigation into their potential for applications in antitumor therapy. Initially, we assessed the endocytosis of

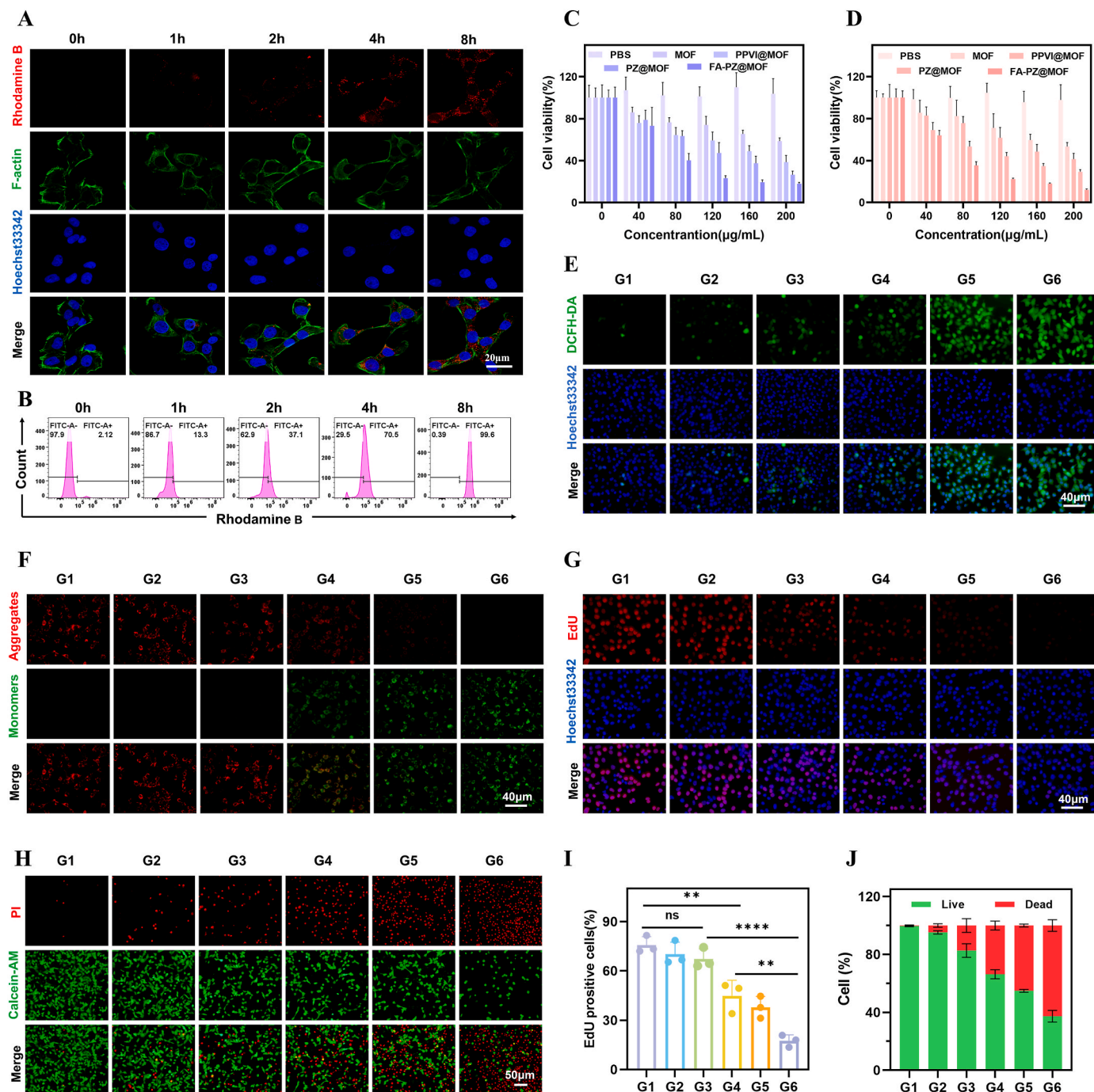


**Fig. 2.** In vitro cellular uptake of FA-PZ@MOF NPs and its synergistic effects on oxidative damage in tumor cells. (A) CLSM images depicting the cellular uptake of Rhodamine B-labeled FA-PZ@MOF NPs at 0, 1, 2, 4 and 8 h post-incubation. (B) Flow cytometry analysis of cellular uptake efficiency of Rhodamine B-labeled FA-PZ@MOF NPs. Cytotoxicity assay of (C) Hepa1-6 cells and (D) Huh-7 cells after treatment with PBS, MOF, PPVI@MOF, PZ@MOF, FA-PZ@MOF NPs at different concentrations for 24 h,  $n = 6$ . (E) Fluorescence microscopy images of Hepa1-6 cells stained with DCFH-DA after different treatments in G1-G6, wherein cell nuclei are stained with Hoechst 33342. (F) Mitochondrial membrane potential changes were detected by JC-1 staining. (G) Fluorescence microscopy images of Hepa1-6 cells after EdU staining in different treatment groups and (I) Semi-quantitative analysis to directly assess cell proliferation. (H) Calcein AM/PI double staining of the Hepa1-6 cells with different treatments and (J) Fluorescence quantification of live/dead cell staining in Hepa1-6,  $n = 3$ . Data are expressed as mean  $\pm$  SD ( $n = 3$ ). One-way Anova or  $t$ -test was used to analyze statistical differences between groups. \* $P < 0.05$ , \*\* $P < 0.01$ , \*\*\* $P < 0.001$ , \*\*\*\* $P < 0.0001$ . "ns" denotes no significant difference. Note, G1: Control, G2: MOF, G3: PPVI, G4: PPVI@MOF, G5: PZ@MOF, G6: FA-PZ@MOF NPs.

rhodamine B-labeled FA-PZ@MOF NPs using Hepa1-6 cells. After incubating the material with Hepa1-6 cells for 1 h, red fluorescence was observed, which reached its maximum intensity after 8 h (Fig. 2A; Fig. S7, Supporting Information), thereby confirming the uptake of FA-PZ@MOF NPs by the Hepa1-6 cells. Additionally, FCM analysis demonstrated that the extent of endocytosis increased progressively with longer incubation times (Fig. 2B).

Next, the cell viability of human normal hepatocytes (THLE-2) was assessed using the CCK-8 assay after 24 h of incubation in a medium containing specific concentrations of FA-PZ@MOF NPs. As shown in Fig. S8 (Supporting Information), high concentrations of the nanomaterials exhibited no significant cytotoxic effects on THLE-2 cells. This phenomenon can be attributed to the neutral microenvironment of normal cells, which enables FA-PZ@MOF NPs to remain relatively stable, further supporting their safety in normal tissues. Subsequently, a CCK-8 assay was conducted on hepatoma tumor cell lines, specifically Hepa1-6 (Fig. 2C) and Huh-7 (Fig. 2D) to evaluate the cytotoxic effects of nanomaterials and validate their efficacy to inhibiting tumor growth. The cells were divided into groups: Control, MOF, PPVI@MOF, PZ@MOF, and FA-PZ@MOF NPs, and incubated for 24 h. Compared with the Control group, the MOF, PPVI@MOF, PZ@MOF, and FA-PZ@MOF NPs groups exhibited significant effects on tumor cells. Cell viability exhibited a decreasing trend as the concentration increased, with the FA-PZ@MOF NPs group showing the most pronounced decrease. Similarly, in the colony formation assay, FA-PZ@MOF NPs demonstrated a superior capacity to inhibit tumor cell proliferation in comparison to the Control group. (Fig. S9, Supporting Information).

In vitro experiments have demonstrated that the production of  $H_2O_2$  can be significantly enhanced by MOF carriers loaded with PPVI and  $ZnO_2$ . To validate the intracellular level of  $H_2O_2$  production, we quantified the concentration of  $H_2O_2$  in Hepa1-6 cells treated with various subgroups (Fig. S10, Supporting Information). The results demonstrated that the intracellular  $H_2O_2$  level in the MOF group was significantly decreased compared to the Control group, attributed to the consumption of  $H_2O_2$  during the Fenton-like reaction. In contrast, the  $H_2O_2$  levels were elevated in Hepa1-6 cells treated with PPVI@MOF, PZ@MOF, and FA-PZ@MOF nanoparticles, owing to the self-supply of  $H_2O_2$  from PPVI and  $ZnO_2$  components. This highlights the self-enhancing CDT efficacy of FA-PZ@MOF nanoparticles. To demonstrate the close association between intracellular  $H_2O_2$  levels and ROS generation, we utilized green fluorescence detection via a DCFH-DA probe to quantify intracellular ROS levels. (Fig. 2E; Fig. S11, Supporting Information). Compared to the Control, MOF, and PPVI groups, the PPVI@MOF, PZ@MOF, and FA-PZ@MOF NPs exhibited markedly enhanced green fluorescence. Indicating that the  $H_2O_2$  supplied by PPVI and  $ZnO_2$  substantially facilitated the generation of  $\bullet OH$  radicals. The FCM results obtained using DCFH-DA were in excellent agreement with the fluorescence microscope images (Fig. S12, Supporting Information). In addition, the depletion of GSH levels in tumor cells leads to elevated oxidative stress, disruption of redox homeostasis, and aggravation of oxidative damage, consequently suppressing tumor cell proliferation. The GSH scavenging capacity of the nanomaterials in tumor cells was assessed using GSH-specific fluorescent probes (Fig. S13, Supporting Information) and GSH/GSSG assay kits (Fig. S14, Supporting Information). The results showed that FA-PZ@MOF NPs rapidly decreased intracellular GSH levels.

The increase in oxidative stress result in the impairment of mitochondrial function. The significant alteration in mitochondrial membrane potential, transitioning from a red fluorescent signal to an intense green fluorescent signal (Fig. 2F), suggests a severe dysfunction of mitochondria. As shown in Fig. S15, treatment with FA-PZ@MOF NPs induced a significant increase in the green fluorescence intensity of Cyt-C, which also indicated the mitochondrial damage. This injury compromised the intracellular ATP production, as illustrated in Fig. S16 (Supporting Information). The minimal ATP content observed in the FA-PZ@MOF NPs group indicated the impaired capacity of tumor cells to generate ATP, thereby hindering the normal efflux of  $Cu^{2+}$  and  $Zn^{2+}$

ions produced during the degradation of FA-PZ@MOF NPs. This led to the accumulation of intracellular  $Cu^{2+}$  and  $Zn^{2+}$  ions, which subsequently expedited mitochondrial dysfunction. Consistent with our hypothesis, a significant correlation was observed between the intracellular accumulation of  $Cu^{2+}$  and  $Zn^{2+}$  ions and mitochondrial damage within the FA-PZ@MOF NPs group. This conclusion was supported by measurements of intracellular Cu concentration following diverse treatments and changes in intracellular zinc levels. (Figure S17 and Figure S18, Supporting Information). Overall, the designed FA-PZ@MOF NPs showed significant potential in inhibiting tumor proliferation owing to their effective cellular uptake, ability to induce oxidative stress, and promotion of mitochondrial dysfunction. This effect was demonstrated in the EdU proliferation assay (Fig. 2G and I). Additionally, to visually assess the antitumor therapeutic efficacy of FA-PZ@MOF NPs, Calcein-AM/PI staining was employed. The images acquired through this staining method demonstrated that the red fluorescence was most intense and the green fluorescence was minimal in the FA-PZ@MOF NPs, further substantiating the significant damage inflicted by FA-PZ@MOF NPs on tumor cells (Fig. 2H and J).

### 3.3. Cuproptosis/pyroptosis/apoptosis induction in vitro

The substantial accumulation of copper ions, the generation of ROS, and the depletion of GSH in tumor cells collectively play a critical role in the initiation and progression of cuproptosis. The central regulator, ferredoxin 1 (FDX1), catalyzes the reduction of  $Cu^{2+}$  to  $Cu^+$ . Excessive intracellular  $Cu^+$  can lead to abnormal aggregation of thioredoxin, which subsequently promotes the oligomerization of Dihydroliipoamide S-acetyltransferase (DLAT). Concurrently lipoyl synthase (LIAS) is downregulation in response to  $Cu^+$  interference. This cascade of events induces a proteotoxic stress response and ultimately triggers cuproptosis in tumor cells [1,7,57,58]. DLAT serves as a critical regulator of cuproptosis in tumor cells. The excessive accumulation of copper ions leads to the oligomerization of DLAT, resulting in an increase in oligomerized DLAT and a decrease in lipoylated DLAT. We validated this hypothesis through Western blot analysis and immunofluorescence staining. As shown in Fig. 3A and B and Figure S19 (Supporting Information), the FA-PZ@MOF group exhibited the weakest fluorescence for lipoylated DLAT and the strongest fluorescence for oligomerized DLAT. The results of Western blot analysis presented in Fig. 3C and Fig. S20 (Supporting Information) demonstrated that the expressions of the cuproptosis-related proteins, including DLAT, LIAS, FDX1 were decreased in G2 compared to G1 and G3. Furthermore, those protein levels were progressively reduced in G4, G5 and G6. These findings suggest that the loading of PPVI enhanced cuproptosis. The decreased expression levels suggest that treatment with FA-PZ@MOF NPs induces proteotoxic stress, thereby leading to cell death and facilitating cuproptosis in tumor cells.

Notably, the disruption of redox balance in cancer cells induced by FA-PZ@MOF NPs further triggered pyroptosis. As revealed by bio-scanning electron microscopy analysis, the cell membranes of the FA-PZ@MOF NPs treated showed partial pore formation, resulting in the leakage of intracellular substances through these pores and the subsequent formation of pyroptotic vesicles (Fig. 3D). When observed under an inverted microscope, the FA-PZ@MOF NPs group showed significant inhibition of Hepa1-6 cell growth following treatment. This was accompanied by a distinct morphological change (Fig. S21), characterized by cell membrane swelling and the formation of prominent air bubbles protruding from the membrane. No significant alterations in the cell morphology were observed in the Control group. And the release of LDH further corroborated of cellular disruption (Fig. S22). This phenomenon, a hallmark of pyroptosis, motivated us to further investigate and validate the mechanism underlying FA-PZ@MOF NPs induced pyroptosis, with specific emphasis on the Caspase-1/GSDMD pathway, which was recognized as the most classical pyroptotic pathway. The excessive accumulation of intracellular oxidative stress and ion overload

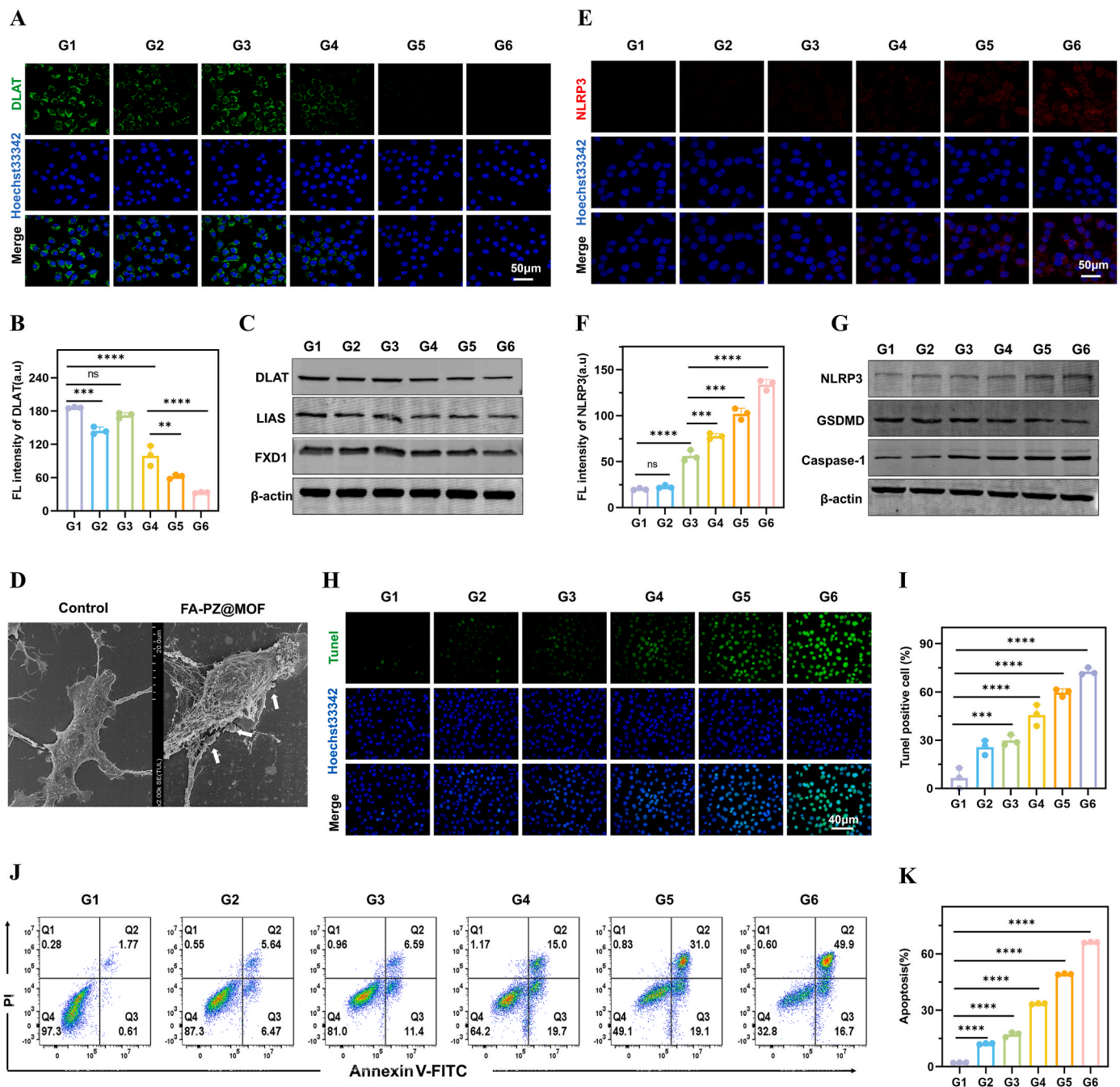


**Fig. 3. In vitro cuproptosis, pyroptosis and apoptosis mechanism studies.** (A) CLSM images of Hepa1-6 cells fluorescence immunostained for DLAT after different treatments; (B) Semi-quantitative analysis of DLAT staining; (C) Western blotting of FDX1, LIAS, and DLAT in Hepa1-6 cells after different treatments. (D) Bio-SEM images of Hepa1-6 cells after treatment with PBS and FA-PZ@MOF NPs for observing cell morphology, wherein the arrows show the outflowed intracellular contents and pyroptotic bodies, Scale bar = 20 nm; (E) CLSM images and (F) Semi-quantitative data of Hepa1-6 cells stained with NLRP3 after different treatments (n = 3); (G) Western blot bands of Caspase-1, GSDMD and NLRP3 in Hepa1-6 cells after different treatments; (H) TUNEL staining images and (I) Fluorescence quantification results demonstrating apoptosis in Hepa1-6 cells treated with various formulations. (J) Flow cytometry patterns and (K) Quantitative data of Hepa1-6 cells stained with propidium iodide (PI) & annexin V-FITC assay kit after different treatments, (n = 3). One-way Anova or t-test was used to analyze statistical differences between groups. \*P < 0.05, \*\*P < 0.01, \*\*\*P < 0.001. "ns" denotes no significant difference. Note, G1: Control, G2: MOF, G3: PPVI, G4: PPVI@MOF, G5: PZ@MOF, G6: FA-PZ@MOF NPs.

can induce the upregulation of NLRP3, subsequently activating Caspase-1 and promoting the cleavage of GSDMD. Immunofluorescence analysis demonstrated an elevated expression of the NLRP3 inflammasome, with the FA-PZ@MOF NPs treated group showing the most intense red fluorescence (Fig. 3E and F). The activation of inflammasomes promotes the activation of Caspase-1, resulting in the upregulation of Caspase-1 protein expression. As a critical protease, Caspase-1 cleaves and

activates proteins within the GSDMD family, releasing its N-terminal domain. The N-terminal domain of GSDMD oligomerizes on the cell membrane, forming a pore-like complex that leads to cell rupture and inducing pyroptosis. This phenomenon was confirmed through the analysis of Western blot data as depicted in Fig. 3G, Figure S23 and Figure S24 (Supporting Information). The expressions of NLRP3, GSDMD, GSDMD-N, Caspase-1 and Cleaved Caspase-1 proteins, which

exhibited no significant differences between the G1 and G2 groups. While with the loading of PPVI and ZnO<sub>2</sub>, the expressions of these proteins in G3, G4, G5, G6 were significantly enhanced or weakened. These findings suggest that PPVI alone is sufficient to induce pyroptosis, and its loading onto the MOF that can induce cuproptosis further amplifies the pyroptosis effect. This evidence demonstrates an interaction between cuproptosis and pyroptosis mediated by FA-PZ@MOF NPs.

To further explore the apoptotic effects of FA-PZ@MOF NPs, we performed TUNEL immunofluorescence staining and observed the brightest green fluorescence in the FA-PZ@MOF NP-treated group, confirming that the effective damage caused by FA-PZ@MOF NPs promoted apoptosis in tumor cells (Fig. 3H and I). Similarly, we performed apoptosis staining of Hepa1-6 cells treated with different nanomaterials using FCM. As shown in Fig. 3J and K, the apoptosis rate in the FA-PZ@MOF NPs group (66.60 %) was significantly higher than that in the PPVI@MOF (34.70 %) and PZ@MOF groups (50.10 %). These results indicate that the FA-PZ@MOF NPs system exerts multiple effects leading to cell death. Taken together, these findings indicate that the designed nanomaterials promote tumor cell death *in vitro* through the induction of cuproptosis, pyroptosis, apoptosis, and other regulatory mechanisms.

### 3.4. Induction of ICD and inhibition of metastasis

The aforementioned experimental results indicated that FA-PZ@MOF NPs can induce tumor apoptosis, cuproptosis, and enhance pyroptosis, suggesting their significant potential to release a large number of DAMPs and thereby induce ICD. The key conditions for the induction of ICD include CRT translocation, HMGB1 secretion, and ATP release. To further validate their effective antitumor immunity, we assessed extracellular ATP levels and found a 14.3-fold increase in the FA-PZ@MOF NP-treated group compared with the control group (Fig. S25, Supporting Information). In addition, the FA-PZ@MOF NPs group showed the strongest red fluorescence on the surface of the cell membrane and the weakest red fluorescence in the nucleus, reflecting the highest levels of CRT exposure and HMGB1 release (Figure S26 and Figure S27, Supporting Information), as further confirmed by Western blot analysis (Fig. S28, Supporting Information). Both the immunofluorescence intensity and Western blot expression of HMGB1 and CRT demonstrated statistically significant differences for G4, G5, and G6 compared to G2 and G3. This indicates that the combination of cuproptosis and pyroptosis can amplify tumor immunity. Besides, FA-PZ@MOF NPs exhibited stronger anti-tumor immune effects under the modification of ZnO<sub>2</sub> and FA.

Relevant studies have shown that cuproptosis and pyroptosis-mediated immunotherapy, along with severe oxidative stress in tumor cells, can effectively suppress the migration and invasion capabilities of tumor cells. First, the inhibitory effect of FA-PZ@MOF NPs on the invasive migration of tumor cells was assessed using a wound-healing assay. It was observed that the Control group exhibited the highest wound healing rate (46.91 %), whereas the FA-PZ@MOF NPs group exhibited the lowest wound healing rate (10.03 %) (Fig. S29, Supporting Information). Second, the migration-inhibiting effect of the nanomaterials on tumor cells was further evaluated by a Transwell assay. The results demonstrated that the lowest tumor migration rate was observed in the FA-PZ@MOF NPs group (Fig. S30, Supporting Information). These results indicate that nanomaterials loaded with PPVI and ZnO<sub>2</sub> promote apoptosis through the functionally impairing tumor-specific ROS storms and mitochondria, effectively inducing ICD, stimulating an immune response, and establishing immune superiority to inhibit tumor metastasis.

### 3.5. *In vivo* distribution, biosafety, and *in vivo* antitumor effect

In the above experiments, we systemically verified the tumor cell targeting, oxidative stress, mitochondrial damage induced by FA-

PZ@MOF NPs, as well as the pronounced effects of cuproptosis, pyroptosis and apoptosis. We further assessed the *in vivo* performance of FA-PZ@MOF NPs. Prior to conducting these *in vivo* experiments, we investigated the *in vivo* biodistribution and tumor accumulation of FA-PZ@MOF NPs in mice. This was achieved by utilizing a small-animal live imaging system to track the distribution of PZ@MOF/Cy5.5 and FA-PZ@MOF/Cy5.5 in a subcutaneous hepatocellular carcinoma tumor model. We injected two sets of NPs (1 mg/mL, 100  $\mu$ L) via caudal vein intravenous injection and conducted fluorescence imaging at various time points to assess the *in vivo* targeting ability of the nanomaterials. Notably, we observed that the nanomaterial FA-PZ@MOF/Cy5.5 began to accumulate at the tumor site 1 h post-injection, and the fluorescence intensity peaking at 12 h after injection, the cumulative fluorescence intensity was significantly higher than that of PZ@MOF/Cy5.5 (Fig. 4A; Fig. S31, Supporting Information). In the distribution analysis of isolated tissues at 24h post-injection, we found that the nanomaterials predominantly accumulated and enriched in the tumor, liver, and lung. FA-PZ@MOF/Cy5.5 showed an approximately 3.97-fold increase in fluorescence signal within the tumor compared to that of PZ@MOF/Cy5.5 (Fig. 4A and B). Furthermore, quantitative analysis was carried out via the ICP-MS technology, more and more FA-PZ@MOF NPs are found to enter and accumulate in tumors within 24 h (Fig. S32, Supporting Information), confirming its effective tumor-targeting ability and anti-tumor therapeutic potential.

Subsequently, the biosafety of FA-PZ@MOF NPs was rigorously evaluated in our experiment. Flowing 14 days of intravenous administration, blood samples were collected for index testing, and hematoxylin and eosin (H&E) staining was conducted on major organs, including the heart, liver, spleen, lungs, and kidneys. *In vivo* biochemical blood analyses revealed that the indices of liver and kidney function in the FA-PZ@MOF NPs group were within normal ranges compared with those in the control group of mice (Fig. S33, Supporting Information). In addition, hemolysis experiments showed that the nanomaterials did not cause significant erythrocyte rupture, even at a concentration of 200  $\mu$ g/mL (Fig. S34, Supporting Information). In conclusion, these findings demonstrate that FA-PZ@MOF NPs possess excellent biocompatibility and biosafety. Thereafter, the antitumor therapeutic efficacy of the nanomaterials was further investigated.

The excellent targeting of FA-PZ@MOF NPs also implied a good therapeutic effect, which was further verified by constructing a subcutaneous tumorigenic model of hepatocellular carcinoma. Once the tumor diameter reached approximately 8 mm, the mice were randomly assigned into six groups: Control, MOF, PPVI, PPVI@MOF, PZ@MOF, and FA-PZ@MOF NPs. The antitumor treatment procedure was illustrated in Fig. 4C, and tumor growth was monitored using animal fluorescence imaging (Fig. 4D). We observed that tumor growth in Group G1 was significantly higher compared to the other groups. In contrast, tumor growth in Groups G2 and G3 was suppressed relative to Group G1 but remained inadequately controlled. These findings suggest that simply enhancing the accumulation of Cu<sup>2+</sup> and utilizing PPVI did not yield a satisfactory therapeutic effect. By evaluating tumor growth dynamics, changes in body weight of mice, collected tumor weights, and the survival rates of the mice (Fig. 4E–H), we demonstrated that the incorporation of PPVI and ZnO<sub>2</sub> into PPVI@MOF and PZ@MOF effectively inhibited tumor growth without causing significant weight loss in the mice. Moreover, the FA-PZ@MOF NPs showed a more potent therapeutic effect, which was largely consistent with the findings from the *in vitro* experiments. Further analysis via H&E staining, Ki67 staining, and TUNEL assays (Fig. 4I) confirmed that treatment with FA-PZ@MOF NPs effectively induced apoptosis and significantly inhibited the proliferation of tumor cells. In addition, Fig. S35 (Supporting Information) presents H&E staining images of major organs (including the heart, liver, spleen, lungs, and kidneys) from each group, showing no damage or necrosis in these organs across all groups. These results further substantiate that the nanomaterials did not exhibit any potential side effects on normal tissue.

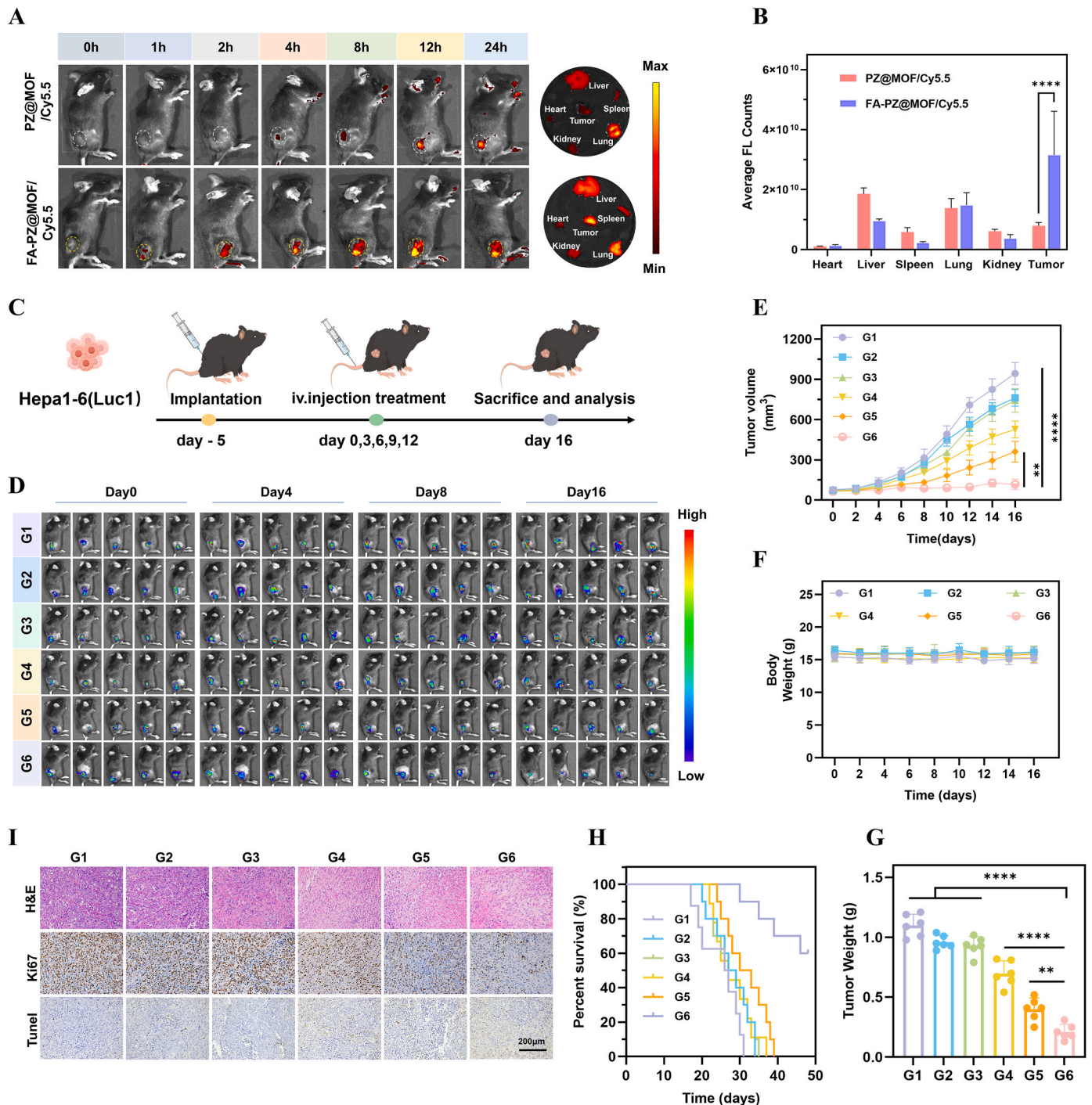


**Fig. 4.** In vivo antitumor evaluations of FA-PZ@MOF NPs. (A) In vivo fluorescence images of tumor-bearing mice after intravenous injection of PZ@MOF/Cy5.5 and FA-PZ@MOF/Cy5.5 and at different time intervals and ex vivo fluorescent image of the dissected organs and tumors at 24 h post-injection. (B) Semi-quantitative analysis of fluorescence intensity in the main organs and harvested tumors ex vivo (n = 3); (C) Schematic on in vivo anti-tumor procedures. (D) In vivo fluorescence images of Luc-Hepa1-6 tumor-bearing mice that experienced different treatments in G1-G6 on Day 0, Day 4, Day 8, and Day 16, where luciferin was administered to illuminate Luc-Hepa1-6 tumor (n = 5). (E) Tumor growth curves of mice post-treatment during 16 days, (n = 6); (F) Time-dependent body weight of mice in G1-G6 (n = 6); (G) Final tumor weight of tumor-bearing mice in G1-G6 (n = 6); (H) Time-dependent survival rate of mice in G1-G6 (n = 10); (I) H&E, Ki67 and TUNEL immunohistochemical images of collected tumor slices in G1-G6 on Day 16. One-way Anova or t-test was used to analyze statistical differences between groups. \*P < 0.05, \*\*P < 0.01, \*\*\*P < 0.001. "ns" denotes no significant difference. Note, G1: Control, G2: MOF, G3: PPVI, G4: PPVI@MOF, G5: PZ@MOF, G6: FA-PZ@MOF NPs.

### 3.6. In vivo antitumor immunotherapy

We investigated the role of FA-PZ@MOF NPs in inducing cuproptosis and pyroptosis in tumor cells in vivo. The expression levels of Caspase-1 and GSDMD were quantitatively evaluated by immunofluorescence staining of tumor tissues. We observed that the treatment with FA-

PZ@MOF NPs significantly enhanced the expression of Caspase-1 while markedly attenuating the expression of GSDMD. (Fig. S36, Supporting Information). Additionally, immunofluorescence staining showed an increase in NLRP3 inflammasomes in tumor tissues, further indicating the successful induction of pyroptosis (Fig. 5A and B). We also observed a significant reduction in DLAT fluorescence in tumor sections

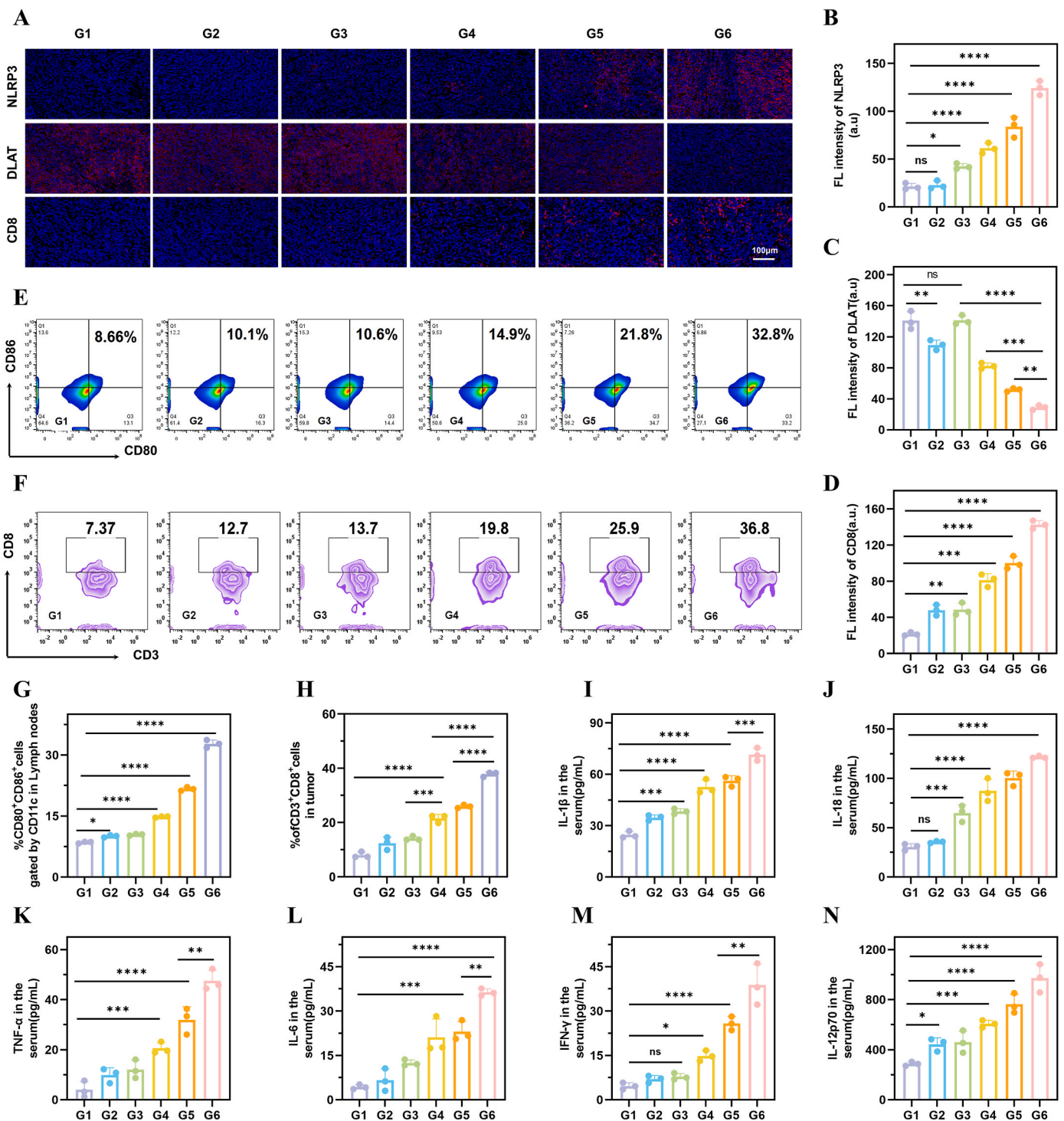


**Fig. 5. In vivo cuproptosis, pyroptosis and immunotherapy analysis.** (A) NLRP3, DLAT and CD8 immunofluorescence images of collected tumor slices in different groups, and semi-quantitative analysis of (B) NLRP3, (C) DLAT, (D) CD8 immunofluorescence staining in Hepa1-6 tumor-bearing mice in vitro. (E) FCM patterns and (G) Quantitative analysis percentages of CD80<sup>+</sup> and CD86<sup>+</sup> cells in CD11c mature dendritic cells in different groups at 16 days after the corresponding treatment (n = 3); (F) FCM patterns and (H) Semi-quantitative analysis percentages of CD8<sup>+</sup> cells among CD3<sup>+</sup> T cells after 16 days of treatment in each group. (n = 3). (I–N) The levels of IL-1β, IL-18, TNF-α, IL-6, IFN-γ and IL-12p70 secretion in mice serum after various treatments (n = 3). One-way Anova or *t*-test was used to analyze statistical differences between groups. \*P < 0.05, \*\*P < 0.01, \*\*\*P < 0.001. "ns" denotes no significant difference. Note, G1: Control, G2: MOF, G3: PPVI, G4: PPVI@MOF, G5: PZ@MOF, G6: FA-PZ@MOF NPs.

from the FA-PZ@MOF NPs group, indicating the effective induction of DLAT depletion and cuproptosis in the tumor tissues (Fig. 5A and C). To further verify the potential immune-activating effects induced by cuproptosis and pyroptosis stimulation, we performed an immunohistochemical assay of CRT expression in tumor tissue sections. Compared

to the control group, the expression level of CRT was significantly elevated in the FA-PZ@MOF NPs group after treatment (Fig. S37, Supporting Information). Moreover, the fluorescence of CD8<sup>+</sup> T cells was significantly enhanced, as evidenced by the immunofluorescence analysis (Fig. 5A and D). This confirms that FA-PZ@MOF NPs can effectively

induce the immune response in the body and enhance the anti-tumor immune efficacy.

Next, we performed FCM assays on lymph nodes and mouse tumors to analyze the maturation of DCs in lymph nodes and the activation levels of T cells. The results showed that treatment with FA-PZ@MOF NPs effectively stimulated the maturation of DCs in the lymph nodes. Specifically, the proportion of CD80<sup>+</sup>CD86<sup>+</sup> cells increased from 8.66 % in the control group to 31.8 % (Fig. 5E and G). Given that the maturation of DCs regulated downstream immune responses by influencing T cell proliferation, we found that treatment with FA-PZ@MOF NPs could recruit cytotoxic T lymphocytes (CD3<sup>+</sup>CD8<sup>+</sup>) infiltration into tumor tissues and upregulate the proportion of CD3<sup>+</sup>CD8<sup>+</sup> cells (Fig. 5F and H). The results suggested that FA-PZ@MOF NPs activate a robust immune response, which can be beneficial for inhibiting tumor cell proliferation and metastasis. In addition, we quantified the serum levels of several key immune-related biomarkers that are indicative of immune cell activation following various treatments. These included cytokines such as IL-1 $\beta$ , IL-18, TNF- $\alpha$ , IL-6, IFN- $\gamma$ , and IL-12p70 (Fig. 5I–N). All of these markers were elevated to varying extents in the FA-PZ@MOF NPs-treated group. The significantly increased expression levels of the cytokines IL-1 $\beta$  and IL-18 in mouse serum, which were associated with pyroptosis, indicated that tumor suppression induced by the nanomaterials was closely linked to the pyroptosis. This finding was consistent with the mechanism of antitumor resistance observed in vitro. Furthermore, the significantly higher concentrations of TNF- $\alpha$  and IL-6 suggested the activation of the immune system. The observed increase in IFN- $\gamma$  indicated that the FA-PZ@MOF NPs stimulated T-cell infiltration and elicited systemic immune responses. Meanwhile, the elevated levels of IL-12p70 indicated the maturation of lymphocytes with the immune system. The aforementioned findings suggested that FA-PZ@MOF nanoparticles can effectively alleviate the immunosuppressive microenvironment, consequently enhancing the anti-tumor efficacy in a significant manner.

#### 4. Conclusions

In this study, we successfully synthesized organometallic framework FA-PZ@MOF nanomaterials to induce cuproptosis and pyroptosis associated immunotherapy. The modification with FA conferred significant targeting ability and biosafety of FA-PZ@MOF NPs. Furthermore, it effectively regulates the tumor microenvironment through GSH depletion, H<sub>2</sub>O<sub>2</sub> generation, and the delivery of Cu<sup>2+</sup> and Zn<sup>2+</sup> ions. After evaluating the excellent performance of FA-PZ@MOF NPs, in vitro experiments showed their remarkable ability in tumor cells to amplify ROS stress, promote mitochondrial damage-induced cuproptosis and pyroptosis, and inhibit tumor migration and invasion. In vivo studies demonstrated that FA-PZ@MOF NPs effectively inhibited subcutaneous tumors and efficiently promoted ICD by inducing a multiple-death strategy, thus triggered a potent antitumor immune response and provided a promising pathway for tumor growth inhibition and immunotherapy in hepatocellular carcinoma.

#### CRediT authorship contribution statement

**Xiaoyuan Yi:** Writing – original draft, Data curation, Conceptualization. **Huaying Xie:** Software, Methodology. **Kunzhaohuang:** Validation, Conceptualization. **Jianzhang Luo:** Investigation, Formal analysis. **Wen Li:** Methodology. **Qingyu Zeng:** Formal analysis. **Feifei He:** Validation. **Wuxiang Shi:** Visualization, Formal analysis. **Duo Wang:** Supervision, Project administration. **Liyan Wang:** Writing – review & editing, Project administration, Funding acquisition, Conceptualization.

#### Informed consent statement

Not applicable.

#### Institutional review board statement

All animal experiments have been approved by Guilin Medical University Ethical Committee with an approval number: GLMC202303112.

#### Funding

This research was funded by National Natural Science Foundation of China, grant number 82173010 and 82402408; Beijing Huatong Guokang Public Welfare Foundation, grant number 2023HT028; Postdoctoral Fellowship Program of CPSF (BX20230068); China Postdoctoral Science Foundation (2024M750452).

#### Declaration of competing interest

The authors declare that they have no known competing financial interests or personal relationships that could have appeared to influence the work reported in this paper.

#### Acknowledgments

We greatly appreciate for the support from Guangxi Clinical Medical Research Center Laboratory of Gastric Cancer.

#### Appendix A. Supplementary data

Supplementary data to this article can be found online at <https://doi.org/10.1016/j.mtbio.2025.101745>.

#### Data availability

The data that support the findings of this study are available from the corresponding author upon reasonable request.

#### References

- [1] Z. Tian, S. Jiang, J. Zhou, W. Zhang, Copper homeostasis and cuproptosis in mitochondria, *Life Sci.* (2023). <https://doi.org/10.1016/j.lfs.2023.122223>.
- [2] J. Xie, Y. Yang, Y. Gao, J. He, Cuproptosis: mechanisms and links with cancers, *Mol. Cancer* (2023). <https://doi.org/10.1186/s12943-023-01732-y>.
- [3] Y. Xu, S.-Y. Liu, L. Zeng, H. Ma, Y. Zhang, H. Yang, Y. Liu, S. Fang, J. Zhao, Y. Xu, C.R. Ashby, Y. He, Z. Dai, Y. Pan, An enzyme-engineered nonporous copper(I) coordination polymer nanoplatfor for cuproptosis-based synergistic cancer therapy, *Adv. Mater.* (2022). <https://doi.org/10.1002/adma.202204733>.
- [4] E.J. Ge, A.I. Bush, A. Casini, P.A. Cobine, J.R. Cross, G.M. DeNicola, Q.P. Dou, K. J. Franz, V.M. Gohil, S. Gupta, S.G. Kaler, S. Lutsenko, V. Mittal, M.J. Petris, R. Polishchuk, M. Ralle, M.L. Schilsky, N.K. Tonks, L.T. Vahdat, L. Van Aelst, D. Xi, P. Yuan, D.C. Brady, C.J. Chang, Connecting copper and cancer: from transition metal signalling to metalloplasia, *Nat. Rev. Cancer* (2021). <https://doi.org/10.1038/s41568-021-00417-2>.
- [5] V. Shanbhag, K. Jasmer-McDonald, S. Zhu, A.L. Martin, N. Gudekar, A. Khan, E. Ladomersky, K. Singh, G.A. Weisman, M.J. Petris, ATP7A delivers copper to the lysyl oxidase family of enzymes and promotes tumorigenesis and metastasis [Cell Biology], *Proc. Natl. Acad. Sci. USA* (2019). <https://doi.org/10.1073/pnas.1817473116>.
- [6] L. Jiasheng, M. Shanshan, L. Qiuhua, W. Qin, Z. Wuning, W. Chunying, L. Junjie, C. Jie, W. Duo, T. Weizhong, L. Tao, Orchestrated copper-loaded nanoreactor for simultaneous induction of cuproptosis and immunotherapeutic intervention in colorectal cancer, *Materials Today Bio* (2024). <https://doi.org/10.1016/j.mtbio.2024.101326>.
- [7] P. Tsvetkov, S. Coy, B. Petrova, M. Dreishpoon, A. Verma, M. Abdusamad, J. Rossen, L. Joesch-Cohen, R. Humeidi, R.D. Spangler, J.K. Eaton, E. Frenkel, M. Kocak, S.M. Corsello, S. Lutsenko, N. Kanarek, S. Santagata, T.R. Golub, Copper induces cell death by targeting lipoylated TCA cycle proteins, *Science* (2022). <https://doi.org/10.1126/science.abf0529>.
- [8] Y. Wu, X. Liu, X. Zhang, S. Zhang, P. Niu, H. Gao, Photothermal theranostics with glutathione depletion and enhanced reactive oxygen species generation for efficient antibacterial treatment, *RSC Adv.* (2023). <https://doi.org/10.1039/d3ra03246a>.
- [9] P. Zhang, C. Zhou, X. Ren, Q. Jing, Y. Gao, C. Yang, Y. Shen, Y. Zhou, W. Hu, F. Jin, H. Xu, L. Yu, Y. Liu, X. Tong, Y. Li, Y. Wang, J. Du, Inhibiting the compensatory elevation of xCT collaborates with disulfiram/copper-induced GSH consumption for cascade ferroptosis and cuproptosis, *Redox Biol.* (2023). <https://doi.org/10.1016/j.redox.2023.103007>.
- [10] S.-R. Li, L.-L. Bu, L. Cai, Cuproptosis: lipoylated TCA cycle proteins-mediated novel cell death pathway, *Signal Transduct. Targeted Ther.* (2022). <https://doi.org/10.1038/s41392-022-01014-x>.

- [11] Y. Qin, Y. Liu, X. Xiang, X. Long, Z. Chen, X. Huang, J. Yang, W. Li, Cuproptosis correlates with immunosuppressive tumor microenvironment based on pan-cancer multiomics and single-cell sequencing analysis, *Mol. Cancer* (2023). [http://10.1186/s12943-023-01752-8](https://doi.org/10.1186/s12943-023-01752-8).
- [12] X. Weijun, S. Aili, A. Abdalrheem Jarelnaby Musa, W. Yaping, F. Jingjing, X. Yuxiang, X. Jiakuan, C. Zhexi, Z. Huichen, Z. Mingzhen, Q. Junmin, Hollow calcium/copper bimetallic amplifier for cuproptosis/paraptosis/apoptosis cancer therapy via cascade reinforcement of endoplasmic reticulum stress and mitochondrial dysfunction, *ACS Nano* (2024). [http://10.1021/acsnano.4c11455](https://doi.org/10.1021/acsnano.4c11455).
- [13] L.-H. Fu, Y. Wan, C. Qi, J. He, C. Li, C. Yang, H. Xu, J. Lin, P. Huang, Nanocatalytic theranostics with glutathione depletion and enhanced reactive oxygen species generation for efficient cancer therapy, *Adv. Mater.* (2021). [http://10.1002/adma.202006892](https://doi.org/10.1002/adma.202006892).
- [14] S. Lu, Y. Li, Y. Yu, Glutathione-scavenging celastrol-Cu nanoparticles induce self-amplified cuproptosis for augmented cancer immunotherapy, *Adv. Mater.* (2024). [http://10.1002/adma.202404971](https://doi.org/10.1002/adma.202404971).
- [15] J. Ding, K. Wang, W. Liu, Y. She, Q. Sun, J. Shi, H. Sun, D.-C. Wang, F. Shao, Pore-forming activity and structural autoinhibition of the gasdermin family, *Nature* (2016). [http://10.1038/nature18590](https://doi.org/10.1038/nature18590).
- [16] F. Shao, Gasdermins: making pores for pyroptosis, *Nat. Rev. Immunol.* (2021). [http://10.1038/s41577-021-00602-2](https://doi.org/10.1038/s41577-021-00602-2).
- [17] H. Zhou, J. He, R. Liu, J. Cheng, Y. Yuan, W. Mao, J. Zhou, H. He, Q. Liu, W. Tan, C. Shuai, Y. Deng, Microenvironment-responsive metal-phenolic network release platform with ROS scavenging, anti-pyroptosis, and ECM regeneration for intervertebral disc degeneration, *Bioact. Mater.* (2024). [http://10.1016/j.bioactmat.2024.02.036](https://doi.org/10.1016/j.bioactmat.2024.02.036).
- [18] M. Li, J. Kim, H. Rha, S. Son, M.S. Levine, Y. Xu, J.L. Sessler, J.S. Kim, Photon-controlled pyroptosis activation (PhotoPyro): an emerging trigger for antitumor immune response, *J. Am. Chem. Soc.* (2023). [http://10.1021/jacs.3c01231](https://doi.org/10.1021/jacs.3c01231).
- [19] X. Liang, D. Wang, Y. Zhao, X. Wang, S. Yao, W. Huang, Y. Yang, X. Dong, L. Zhang, J. Yang, Tumor microenvironment-responsive manganese-based nano-modulator activate the cGAS-STING pathway to enhance innate immune system response, *J. Nanobiotechnol.* (2024). [http://10.1186/s12951-024-02809-6](https://doi.org/10.1186/s12951-024-02809-6).
- [20] S. Zhang, Y. Zhang, Y. Feng, J. Wu, Y. Hu, L. Lin, C. Xu, J. Chen, Z. Tang, H. Tian, X. Chen, Biomimetic two-enzyme nanoparticles regulate tumor glycometabolism inducing tumor cell pyroptosis and robust antitumor immunotherapy, *Adv. Mater.* (2022). [http://10.1002/adma.202206851](https://doi.org/10.1002/adma.202206851).
- [21] Q. Chen, Y. Sun, S. Wang, J. Xu, New prospects of cancer therapy based on pyroptosis and pyroptosis inducers, *Apoptosis* (2023). [http://10.1007/s10495-023-01906-5](https://doi.org/10.1007/s10495-023-01906-5).
- [22] L. Yu, Y. Xu, Z. Pu, H. Kang, M. Li, J.L. Sessler, J.S. Kim, Photocatalytic superoxide radical generator that induces pyroptosis in cancer cells, *J. Am. Chem. Soc.* (2022). [http://10.1021/jacs.2c03256](https://doi.org/10.1021/jacs.2c03256).
- [23] X. Liu, Z. Zhang, J. Ruan, Y. Pan, V.G. Magupalli, H. Wu, J. Lieberman, Inflammasome-activated gasdermin D causes pyroptosis by forming membrane pores, *Nature* (2016). [http://10.1038/nature18629](https://doi.org/10.1038/nature18629).
- [24] W. Zhang, Z. Liu, J. Zhu, Z. Liu, Y. Zhang, G. Qin, J. Ren, X. Qu, Bioorthogonal disruption of pyroptosis checkpoint for high-efficiency pyroptosis cancer therapy, *J. Am. Chem. Soc.* (2023). [http://10.1021/jacs.3c04180](https://doi.org/10.1021/jacs.3c04180).
- [25] D. Wang, T. Nie, C. Huang, Z. Chen, X. Ma, W. Fang, Y. Huang, L. Luo, Z. Xiao, Metal-cyclic dinucleotide nanomodulator-stimulated STING signaling for strengthened radioimmunotherapy of large tumor, *Small* (2022). [http://10.1002/smll.202203227](https://doi.org/10.1002/smll.202203227).
- [26] W. Wang, L. Zhang, Y. Zhang, X. Liu, A. Song, J. Ren, X. Qu, A self-adaptive pyroptosis inducer: optimizing the catalytic microenvironment of nanozymes by membrane-adsorbed microbe enables potent cancer immunotherapy, *Adv. Mater.* (2023). [http://10.1002/adma.202310063](https://doi.org/10.1002/adma.202310063).
- [27] B. Ye, W. Hu, G. Yu, H. Yang, B. Gao, J. Ji, Z. Mao, F. Huang, W. Wang, Y.A. Ding, Cascade-amplified pyroptosis inducer: optimizing oxidative stress microenvironment by self-supplying reactive nitrogen species enables potent cancer immunotherapy, *ACS Nano* (2024). [http://10.1021/acsnano.4c03172](https://doi.org/10.1021/acsnano.4c03172).
- [28] Y. Hekai, X. Guangzhao, L. Fahui, G. Guanhong, Y. Ping, C. Yuxi, C. Yongkang, S. Wen, S. Weiguo, Z. Wenda, Multi-enzyme nanoparticles as efficient pyroptosis and immunogenic cell death inducers for cancer immunotherapy, *Adv. Sci.* (2024). [http://10.1002/adv.202408729](https://doi.org/10.1002/adv.202408729).
- [29] H. Ren, Z. Wu, J. Tan, H. Tao, W. Zou, Z. Cao, B. Wen, Z. Cai, J. Du, Z. Deng, Co-Delivery nano system of MS-275 and V-9302 induces pyroptosis and enhances anti-tumor immunity against uveal melanoma, *Adv. Sci.* (2024). [http://10.1002/adv.202404375](https://doi.org/10.1002/adv.202404375).
- [30] Y. Liu, R. Niu, X. Zhang, B. Zhang, X. Chen, J. Guo, S. Song, Y. Wang, H. Zhang, Y. Zhao, Metal-organic framework-based nanovaccine for relieving immunosuppressive tumors via hindering efferocytosis of macrophages and promoting pyroptosis and cuproptosis of cancer cells, *ACS Nano* (2024). [http://10.1021/acsnano.4c01518](https://doi.org/10.1021/acsnano.4c01518).
- [31] Y.-Y. Wang, S.-L. Li, X.-Y. Zhang, F.-L. Jiang, Q.-L. Guo, P. Jiang, Y. Liu, "Multi-in-One" yolk-shell structured nanoplatfor inducing pyroptosis and antitumor immune response through cascade reactions, *Small* (2024). [http://10.1002/smll.202400254](https://doi.org/10.1002/smll.202400254).
- [32] L. Qiao, G. Zhu, T. Jiang, Y. Qian, Q. Sun, G. Zhao, H. Gao, C. Li, Self-destructive copper carriers induce pyroptosis and cuproptosis for efficient tumor immunotherapy against dormant and recurrent tumors, *Adv. Mater.* (2023). [http://10.1002/adma.202308241](https://doi.org/10.1002/adma.202308241).
- [33] Y. Li, Y. Guo, K. Zhang, R. Zhu, X. Chen, Z. Zhang, W. Yang, Cell death pathway regulation by functional nanomedicines for robust antitumor immunity, *Adv. Sci.* (2023). [http://10.1002/adv.202306580](https://doi.org/10.1002/adv.202306580).
- [34] Y. Huang, X. Liu, J. Zhu, Z. Chen, L. Yu, X. Huang, C. Dong, J. Li, H. Zhou, Y. Yang, W. Tan, Enzyme core spherical nucleic acid that enables enhanced cuproptosis and antitumor immune response through alleviating tumor hypoxia, *J. Am. Chem. Soc.* (2024). [http://10.1021/jacs.3c14247](https://doi.org/10.1021/jacs.3c14247).
- [35] G. Zhu, M. Wang, L. Qiao, Y. Xie, J. Wang, L. Li, Q. Sun, P. Zheng, C. Li, Lysosomal rupture-mediated "broken window effect" to amplify cuproptosis and pyroptosis for high-efficiency cancer immunotherapy, *Adv. Funct. Mater.* (2024). [http://10.1002/adfm.202400496](https://doi.org/10.1002/adfm.202400496).
- [36] Z. Guoqing, X. Yulin, W. Junrong, W. Man, Q. Yanrong, S. Qianqian, D. Yunlu, L. Chunxia, Multifunctional copper-phenolic nanopills achieve comprehensive polyamines depletion to provoke enhanced pyroptosis and cuproptosis for cancer immunotherapy, *Adv. Mater.* (2024). [http://10.1002/adma.202409066](https://doi.org/10.1002/adma.202409066).
- [37] L. Jiayi, Z. Kaifan, L. Luping, Z. Mengdi, Z. Ziqi, C. Junyu, L. Shaoguang, Y. Hong, L. Ailin, L. Xinhua, L. Gang, C. Bing, Reprogramming the tumor immune microenvironment through activatable photothermal therapy and GSH depletion using liposomal gold nanocages to potentiate anti-metastatic immunotherapy, *Small* (2024). [http://10.1002/smll.202407388](https://doi.org/10.1002/smll.202407388).
- [38] S. Peng, F. Xiao, M. Chen, H. Gao, Tumor-microenvironment-responsive nanomedicine for enhanced cancer immunotherapy, *Adv. Sci.* (2021). [http://10.1002/adv.202103836](https://doi.org/10.1002/adv.202103836).
- [39] M.A. Beach, U. Nayanathara, Y. Gao, C. Zhang, Y. Xiong, Y. Wang, G.K. Such, Polymeric nanoparticles for drug delivery, *Chem. Rev.* (2024). [http://10.1021/acs.chemrev.3c00705](https://doi.org/10.1021/acs.chemrev.3c00705).
- [40] J. Zhang, Y. Lin, Z. Lin, Q. Wei, J. Qian, R. Ruan, X. Jiang, L. Hou, J. Song, J. Ding, H. Yang, Stimuli-responsive nanoparticles for controlled drug delivery in synergistic cancer immunotherapy, *Adv. Sci.* (2021). [http://10.1002/adv.202103444](https://doi.org/10.1002/adv.202103444).
- [41] G. Kroemer, L. Galluzzi, O. Kepp, L. Zitvogel, Immunogenic cell death in cancer therapy, *Annu. Rev. Immunol.* (2012). [http://10.1146/annurev-immunol-032712-100008](https://doi.org/10.1146/annurev-immunol-032712-100008).
- [42] Z. Li, X. Lai, S. Fu, L. Ren, H. Cai, H. Zhang, Z. Gu, X. Ma, K. Luo, Immunogenic cell death activates the tumor immune microenvironment to boost the immunotherapy efficiency, *Adv. Sci.* (2022). [http://10.1002/adv.202201734](https://doi.org/10.1002/adv.202201734).
- [43] W. Xu, J. Qian, G. Hou, T. Wang, J. Wang, Y. Wang, L. Yang, X. Cui, A. Suo, A hollow amorphous bimetal organic framework for synergistic cuproptosis/ferroptosis/apoptosis anticancer therapy via disrupting intracellular redox homeostasis and copper/iron metabolisms, *Adv. Funct. Mater.* (2022). [http://10.1002/adfm.202205013](https://doi.org/10.1002/adfm.202205013).
- [44] Z. Fan, S. Wu, H. Deng, G. Li, L. Huang, H. Liu, Light-triggered nanozymes remodel the tumor hypoxic and immunosuppressive microenvironment for ferroptosis-enhanced antitumor immunity, *ACS Nano* (2024). [http://10.1021/acsnano.4c00844](https://doi.org/10.1021/acsnano.4c00844).
- [45] D. Wang, X. Zhu, X. Wang, Q. Wang, K. Yan, G. Zeng, G. Qiu, R. Jiao, X. Lin, J. Chen, Q. Yang, W. Qin, J. Liu, K. Zhang, Y. Liu, Multichannel sonocatalysis amplifiers target IDH1-mutated tumor plasticity and attenuate ros tolerance to repress malignant cholangiocarcinoma, *Adv. Funct. Mater.* (2023). [http://10.1002/adfm.202303869](https://doi.org/10.1002/adfm.202303869).
- [46] T. Yang, S. Zhang, H. Yuan, Y. Wang, L. Cai, H. Chen, X. Wang, D. Song, X. Wang, Z. Guo, X. Zhang, Platinum-based TREM2 inhibitor suppresses tumors by remodeling the immunosuppressive microenvironment, *Angew. Chem. Int. Ed.* (2022). [http://10.1002/anie.202213337](https://doi.org/10.1002/anie.202213337).
- [47] Z. Xiaoqi, L. Tinghua, W. Qin, Y. Kangning, M. Shanshan, L. Yuan, Z. Guichun, L. Junjie, C. Jun, W. Duo, Dual-synergistic nanomodulator alleviates exosomal PD-L1 expression enabling exhausted cytotoxic T lymphocytes rejuvenation for potentiated irFA-treated hepatocellular carcinoma immunotherapy, *ACS Nano* (2024). [http://10.1021/acsnano.4c11257](https://doi.org/10.1021/acsnano.4c11257).
- [48] W. Xu, Y. Wang, G. Hou, J. Wang, T. Wang, J. Qian, A. Suo, Tumor microenvironment responsive hollow nanoplatfor for triple amplification of oxidative stress to enhance cuproptosis-based synergistic cancer therapy, *Adv. Healthcare Mater.* (2023). [http://10.1002/adhm.202202949](https://doi.org/10.1002/adhm.202202949).
- [49] C. Yu, J. Li, P. Zang, L. Feng, B. Tian, R. Zhao, Y. Xie, L. Wu, Z. Chen, P. Yang, A functional "key" amplified piezoelectric effect modulates ROS storm with an open source for multimodal synergistic cancer therapy, *Small* (2024). [http://10.1002/smll.202401931](https://doi.org/10.1002/smll.202401931).
- [50] W. Li, Y. Xiao, G. Guo, J. Peng, N. Zhu, Z. Chen, B. Peng, Z. Jiang, B. Li, G. Yu, Z. Guo, M. Liang, W. Guo, Cuprous oxide nanocomposites with photothermal (PTT) and chemical dynamics (CDT) effects induce cuproptosis in breast cancer using the strategy of increasing inflow and reducing outflow, *Nano Today* (2024). [http://10.1016/j.nantod.2024.102223](https://doi.org/10.1016/j.nantod.2024.102223).
- [51] W. Pi, L. Wu, J. Lu, X. Lin, X. Huang, Z. Wang, Z. Yuan, H. Qiu, J. Zhang, H. Lei, P. Wang, A metal ions-mediated natural small molecules carrier-free injectable hydrogel achieving laser-mediated photo-Fenton-like anticancer therapy by synergy apoptosis/cuproptosis/anti-inflammation, *Bioact. Mater.* (2023). [http://10.1016/j.bioactmat.2023.06.018](https://doi.org/10.1016/j.bioactmat.2023.06.018).
- [52] W. Xiao, K. Qu, W. Zhang, L. Lai, L. He, F. Cheng, L. Wang, High immunogenic cuproptosis evoked by in situ sulfidation-activated pyroptosis for tumor-targeted immunotherapy of colorectal cancer, *Small Science* (2024). [http://10.1002/smsc.202300164](https://doi.org/10.1002/smsc.202300164).
- [53] J. Zhong, X.-C. Lu, X. Zheng, R.K. Kankala, S.-B. Wang, A.-Z. Chen, Inducing pyroptosis and cuproptosis using copper carriers for ROS-augmented effective cancer therapy, *ACS Mater. Lett.* (2024). [http://10.1021/acsmaterialslett.4c01142](https://doi.org/10.1021/acsmaterialslett.4c01142).
- [54] J.-F. Teng, Q.-B. Mei, X.-G. Zhou, Y. Tang, R. Xiong, W.-Q. Qiu, R. Pan, B.Y.-K. Law, V.K.-W. Wong, C.-L. Yu, H.-A. Long, X.-L. Xiao, F. Zhang, J.-M. Wu, D.-L. Qin, A.-G. Wu, Polyphyllin VI induces caspase-1-mediated pyroptosis via the induction of

- ROS/NF- $\kappa$ B/NLRP3/GSDMD signal Axis in non-small cell lung cancer, *Cancers* (2020). <http://10.3390/cancers12010193>.
- [55] C. Zhang, Q. Li, G. Qin, Y. Zhang, C. Li, L. Han, R. Wang, S. Wang, H. Chen, K. Liu, C. He, Anti-angiogenesis and anti-metastasis effects of Polyphyllin VII on Hepatocellular carcinoma cells in vitro and in vivo, *Chin. Med.* (2021). <http://10.1186/s13020-021-00447-w>.
- [56] Q. Liu, L.-N. Jin, W.-Y. Sun, Facile fabrication and adsorption property of a nano/microporous coordination polymer with controllable size and morphology, *Chem. Commun.* (2012). <http://10.1039/c2cc34192a>.
- [57] Z. Min, M. Faheem, Z. Yihong, L. Tong, F. Jiayuan, Z. Jingyuan, W. Hui, Copper depletion-induced tumor cuproptosis, *Chem. Sci.* (2024). <http://10.1039/d4sc04712e>.
- [58] L. You, W. Dongmei, G. Chenglu, W. Xue, Z. Shuang, Z. Ziyue, Z. Fuquan, Y. Junfang, G. Zhanjun, A cuproptosis nanocapsule for cancer radiotherapy, *Nat. Nanotechnol.* (2024). <http://10.1038/s41565-024-01784-1>.